Article

The Fabrication and Property Characterization of a Ho$_2$YSbO$_7$/Bi$_2$MoO$_6$ Heterojunction Photocatalyst and the Application of the Photodegradation of Diuron under Visible Light Irradiation

Liang Hao [1] and Jingfei Luan [1,2,*]

[1] School of Physics, Changchun Normal University, Changchun 130032, China; hliang0725@163.com
[2] State Key Laboratory of Pollution Control and Resource Reuse, School of the Environment, Nanjing University, Nanjing 210093, China
* Correspondence: jfluan@nju.edu.cn; Tel.: +86-19951939498

Abstract: A novel photocatalytic nanomaterial, Ho$_2$YSbO$_7$, was successfully synthesized for the first time using the solvothermal synthesis technique. In addition, a Ho$_2$YSbO$_7$/Bi$_2$MoO$_6$ heterojunction photocatalyst (HBHP) was prepared via the hydrothermal fabrication technique. Extensive characterizations of the synthesized samples were conducted using various instruments, such as an X-ray diffractometer, a Fourier transform infrared spectrometer, a Raman spectrometer, a UV-visible spectrophotometer, an X-ray photoelectron spectrometer, and a transmission electron microscope, as well as X-ray energy dispersive spectroscopy, photoluminescence spectroscopy, a photocurrent test, electrochemical impedance spectroscopy, ultraviolet photoelectron spectroscopy, and electron paramagnetic resonance. The photocatalytic activity of the HBHP was evaluated for the degradation of diuron (DRN) and the mineralization of total organic carbon (TOC) under visible light exposure for 152 min. Remarkable removal efficiencies were achieved, with 99.78% for DRN and 97.19% for TOC. Comparative analysis demonstrated that the HBHP exhibited markedly higher removal efficiencies for DRN compared to Ho$_2$YSbO$_7$, Bi$_2$MoO$_6$, or N-doped TiO$_2$ photocatalyst, with removal efficiencies 1.13 times, 1.21 times, or 2.95 times higher, respectively. Similarly, the HBHP demonstrated significantly higher removal efficiencies for TOC compared to Ho$_2$YSbO$_7$, Bi$_2$MoO$_6$, or N-doped TiO$_2$ photocatalyst, with removal efficiencies 1.17 times, 1.25 times, or 3.39 times higher, respectively. Furthermore, the HBHP demonstrated excellent stability and reusability. The mechanisms which could enhance the photocatalytic activity remarkably and the involvement of the major active species were comprehensively discussed, with superoxide radicals identified as the primary active species, followed by hydroxyl radicals and holes. The results of this study contribute to the advancement of efficient heterostructural materials and offer valuable insights into the development of sustainable remediation strategies for addressing DRN contamination.

Keywords: Ho$_2$YSbO$_7$; Ho$_2$YSbO$_7$/Bi$_2$MoO$_6$ heterojunction photocatalyst; diuron; visible light exposure; photocatalytic activity; degradation pathway; degradation mechanism

1. Introduction

To address the pressing issue of food scarcity resulting from population growth and limited agricultural resources, the use of pesticides has become indispensable in enhancing crop yield [1–3]. Among various pesticides, diuron (DRN) stands out as a widely utilized herbicide due to its universality and effectiveness at weed control [4–6]. However, the residual presence of DRN in agricultural production poses significant risks to organisms due to its carcinogenic and genotoxic properties [7,8]. Recognizing its potential harm, the European Union's Water Framework Directive designated DRN as a hazardous substance, and the United States Environmental Protection Agency classified it as a "known probable"

human carcinogen [9]. In order to mitigate the negative effects of DRN on water resources and organisms, it is imperative to degrade DRN in pesticide wastewater into mineral or relatively stable innoxious organic solids.

The traditional process of water pollution treatment involved the fusion of physical, chemical, and biological methods [10–12]. Nonetheless, with the advancement of industrial processes, effluents have become increasingly complex, making it more challenging to completely remove organic pollutants using these conventional methods. Moreover, these conventional methods suffer from issues such as incomplete degradation, low efficiency, high cost, and the potential for secondary pollution risks [13–15]. Thus, additional treatment steps should be incorporated into effluent treatment projects to ensure the further removal of toxic materials.

Semiconductor photocatalysis technology, recognized as an advanced oxidation process (AOP), has emerged as a highly promising and effective approach for water pollution treatment [16–19]. Its notable advantages include low cost, high efficiency, absence of secondary pollution, recyclability, and environmentally friendly characteristics [20–22]. By harnessing solar energy, semiconductor photocatalysis successfully degraded highly stable organic molecules, addressing the persistent challenge of water pollution. During the photocatalytic process, semiconductor photocatalysts are excited by solar radiation, resulting in the generation of electron–hole pairs. These pairs further produce reactive oxygen species (ROS) such as hydroxyl and superoxide radicals, which facilitate the oxidation process of pollutants, ultimately mineralizing them into innocuous CO_2 and H_2O [23–25]. While ultraviolet light constitutes only 5% of solar radiation, visible light represents a larger portion, accounting for 45% of solar energy. However, traditional semiconductor photocatalysts such as titanium dioxide and zinc oxide require ultraviolet or near-ultraviolet radiation for activation, resulting in a significant waste of energy [26–30]. Hence, synthesizing composite photocatalytic materials is crucial for effectively utilizing solar energy as composite catalysts have shown significant improvements in terms of sunlight absorption range and photocatalytic capability compared to single metal oxide catalysts [31,32]. Previous studies have demonstrated the favorable photocatalytic capability of $A_2B_2O_7$ and AB_2O_6 mixtures under visible light exposure (VLE) [33–39]. For instance, Devi et al. achieved a photocatalytic removal efficiency (REF) of 66% for methylene blue (0.1 mmol/L) using the photocatalyst $YGdTi_2O_7$ under VLE for 180 min [40]. Similarly, Zhang et al. reported an REF of 69.7% for methyl orange (20 mg/L) using the photocatalyst $Gd_2Ce_2O_7$ powder under VLE for 300 min [41]. Furthermore, Bi_2MoO_6, an important Aurivillius-phase perovskite, has garnered great attention for its excellent photocatalytic activity under VLE [42,43]. Zhao et al. found that Bi_2MoO_6 powder achieved an REF of 65.6% for methyl blue (20 mg/L) under VLE for 240 min, while Li et al. demonstrated a photocatalytic REF of 60% for rhodamine B (10 mg/L) using Bi_2MoO_6 under VLE for 120 min [44,45]. Building upon these promising findings, we have integrated Bi_2MoO_6 into our latest research to develop a novel photocatalytic material that exhibited enhanced performance for water pollution treatment. Further details will be elaborated in the subsequent sections.

In our previous research, we extensively explored the potential for structure tuning in the stable pyrochlore-structured photocatalyst Bi_2InTaO_7 [46]. The groundbreaking research conducted by Barrocas et al. has demonstrated remarkable photocatalytic degradation efficiencies for methylene blue dye pollutants using Bi_2S_3–ZnS/TNF nanocomposite photocatalytic materials, as well as for Rhodamine 6G dye pollutants using $Ca_{1-x}Ln_xMnO_3$ and $Ca_{0.6}Ho_{0.4}MnO_3$ film photocatalytic materials [47–49]. These remarkable findings have served as a significant source of inspiration for our own research. Moreover, the advancements made by Cai et al. in the degradation of methyl orange dye utilizing Ho-doped TiO_2 photocatalysts have also been highly beneficial to our work [50]. Expanding on the above analysis, we hypothesized that the carrier concentration could be enhanced through specific element substitutions. Experimental results confirmed the advanced photocatalytic potential of the novel photocatalyst Ho_2YSbO_7.

To further enhance the efficacy of photocatalysts, various methods have been explored, including morphological control, band gap engineering, and the construction of heterojunction structures [51–54]. Among these techniques, the construction of heterojunction photocatalysts has garnered significant attention [55,56]. The formation of a strong internal electric field within heterojunction photocatalytic materials effectively separated and transferred photoinduced carriers (PICs), thereby reducing their recombination reactions [57,58]. This promoted the generation of ROS, ultimately reinforcing the photocatalytic capability of the catalyst [16]. In recent years, substantial progress has been made in the field of semiconductor heterojunction photocatalysts. For instance, Luo et al. reported on the construction of a SnS_2/Ag_3PO_4 heterojunction photocatalyst, which exhibited enhanced degradation performance compared to individual SnS_2 and Ag_3PO_4 catalysts [59]. Similarly, Zhang et al. demonstrated an improved photodegradation rate of tetracycline hydrochloride using a g-C_3N_4/TiO_2 heterojunction photocatalyst compared to each standalone catalyst [60].

Motivated by these fundamental insights, we have developed a novel heterostructure photocatalytic material, Ho_2YSbO_7/Bi_2MoO_6, for the effective removal of DRN from pesticide wastewater under VLE. Experimental results confirmed the exceptional performance of the Ho_2YSbO_7/Bi_2MoO_6 heterojunction photocatalyst (HBHP), achieving a remarkable DRN (0.032 mmol/L) REF of 99.78% within 152 min of VLE. The remarkable superiority of HBHP was evident in its exceptional performance compared to conventional TiO_2. Within the same irradiation time, TiO_2 achieved a removal efficiency of less than 40% for a DRN initial concentration of 0.0043 mmol/L under UV light condition [61]. Similarly, the nickel organic xerogel achieved a removal efficiency of less than 80% for a DRN initial concentration of 0.021 mmol/L under simulated sunlight conditions [62]. These striking disparities clearly demonstrate the significantly enhanced effectiveness of the tested photocatalyst in degrading DRN. Additionally, the photocatalytic degradation efficiency of DRN in pesticide wastewater under VLE was evaluated for various photocatalysts, including HBHP, Ho_2YSbO_7, Bi_2MoO_6, and nitrogen-doped titanium dioxide. This study presents a significant innovation by successfully synthesizing the novel visible-light-driven Ho_2YSbO_7 photocatalytic material with excellent photocatalytic properties using the solvothermal synthesis technique. These findings represent a remarkable advancement in the development of efficient and environmentally friendly photocatalytic systems for DRN degradation in pesticide wastewater.

2. Result and Discussion

2.1. X-ray Diffraction Analysis

Figure 1 presents the XRD patterns of the HBHP, Ho_2YSbO_7, and Bi_2MoO_6. The observed peaks and crystal planes in the XRD pattern of the HBHP match those of Ho_2YSbO_7 and Bi_2MoO_6, affirming the successful synthesis of the HBHP [63–65]. To verify the crystal structures, the XRD data of Ho_2YSbO_7 and Bi_2MoO_6 were further subjected to Rietveld refinement using the Materials Studio program, as shown in Figures 2a and 3a, respectively. The refined results for Ho_2YSbO_7 (R_P = 5.45%) and Bi_2MoO_6 (R_P = 6.29%) exhibit exceptional agreement between the experimental and theoretical intensities. This confirms the pyrochlore-type structure of Ho_2YSbO_7 and the structural arrangement of Bi_2MoO_6, consisting of $(MoO_4)^{2-}$ perovskite layers organized between $(Bi_2O_2)^{2+}$ layers [42,66]. Moreover, both compounds exhibit single-phase behavior, with Ho_2YSbO_7 crystallizing in the cubic crystal system with the space group Fd3m and Bi_2MoO_6 adopting the orthorhombic crystal system with the space group Pca21. The lattice constant of Ho_2YSbO_7 was determined to be 10.355 Å, and for Bi_2MoO_6, the lattice constants were found to be a = 5.432 Å, b = 16.370 Å, and c = 5.447 Å. The refinement model, which accounted for the presence of oxygen atoms, demonstrates excellent agreement between the experimental and theoretical intensities. Additionally, the XRD pattern of N-doped TiO_2 (NTO) is depicted in Figure S1, showing the characteristic lattice planes of the anatase phase of TiO_2 (JCPDS No. 21-1272) [67–69].

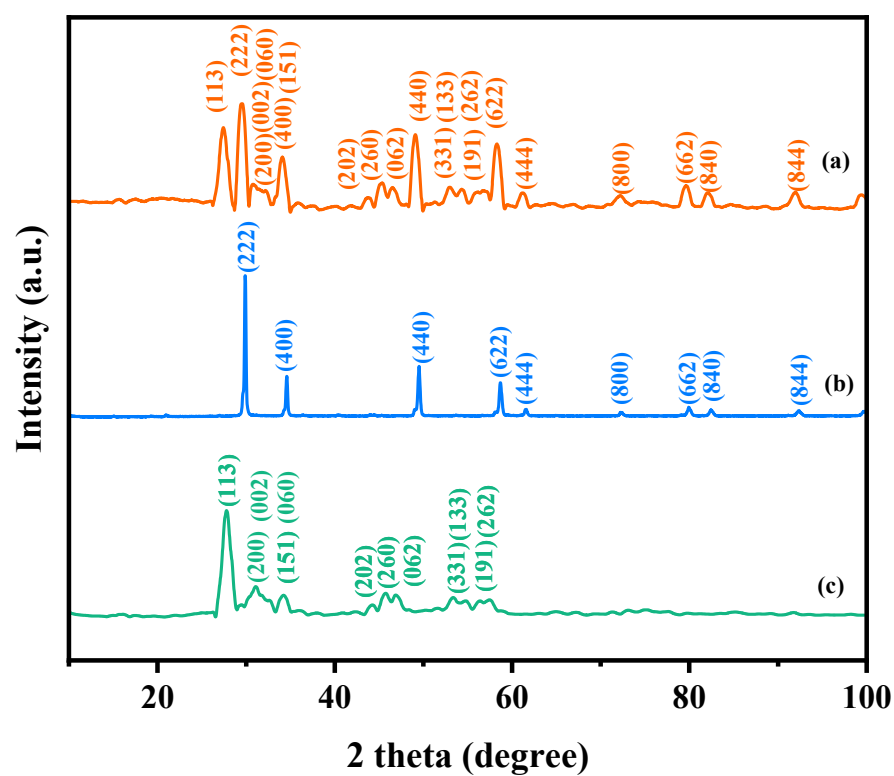**Figure 1.** XRD imageries: (**a**) HBHP, (**b**) Ho_2YSbO_7, and (**c**) Bi_2MoO_6.
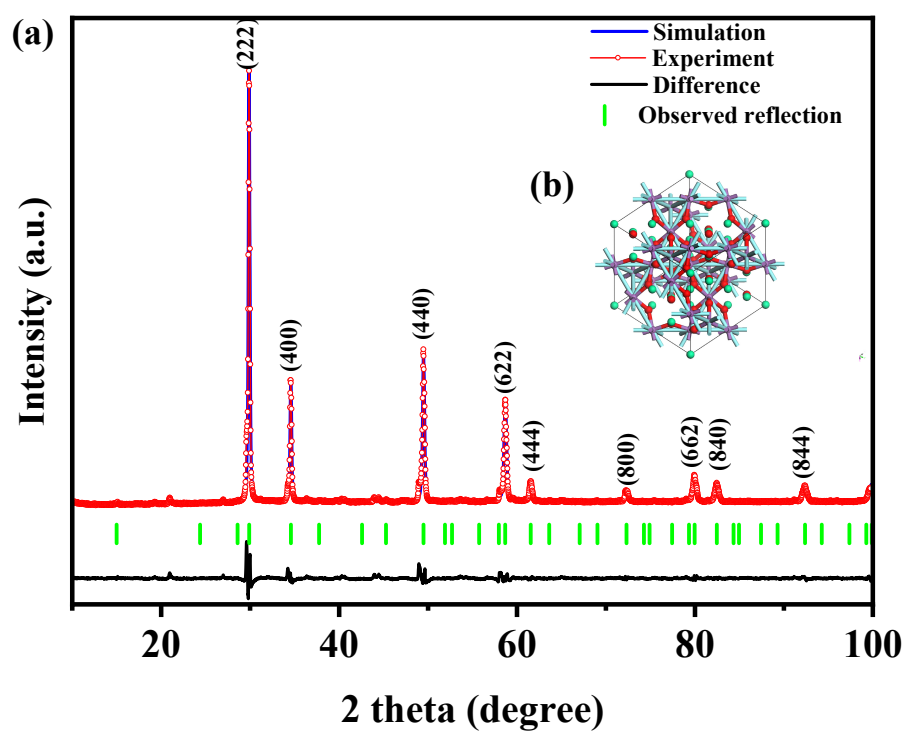

Figure 2. (**a**) XRD imagery and Rietveld refinement and (**b**) the atomic structure (red atom: O; cyan atom: Y or Sb; green atom: Ho) of Ho_2YSbO_7.

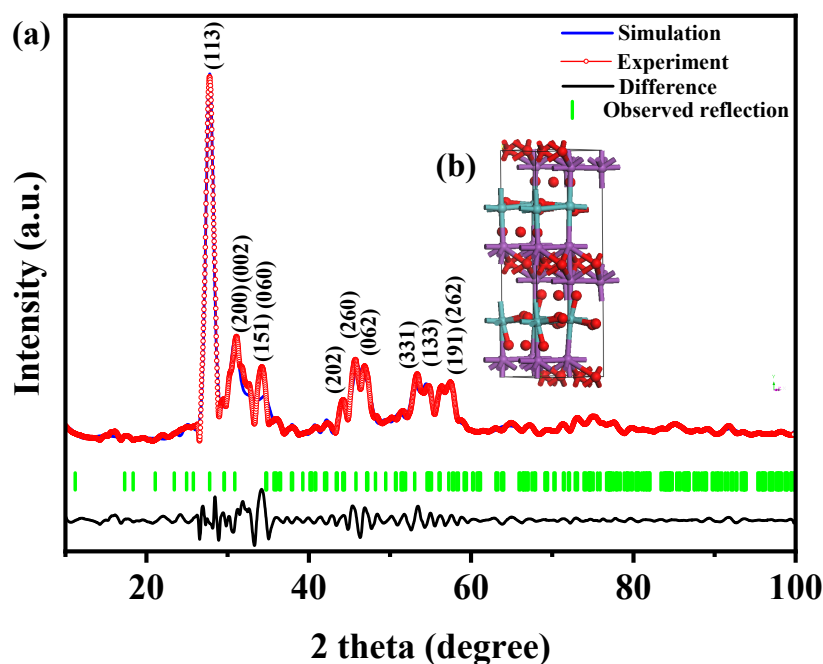**Figure 3.** (**a**) XRD pattern and Rietveld refinement and (**b**) the atomic structure (Red atom: O; blue atom: Mo; purple atom: Bi) of Bi_2MoO_6.

Figures 2b and 3b illustrate the atomic structures of Ho_2YSbO_7 and Bi_2MoO_6, respectively. These crystal structures were constructed by us using the corresponding space group, crystal system, lattice constants, atomic coordinates, and structural parameters. Furthermore, Tables 1 and 2 present the atomic coordinates and structural parameters for Ho_2YSbO_7 and Bi_2MoO_6, respectively [70,71]. These detailed analyses provide strong evidence for the structural stability of the synthesized compounds and underscore their potential as highly efficient photocatalysts in various applications.

Table 1. Structural eigenvalues of Ho_2YSbO_7 fabricated by solvothermal synthesis technique.

Atom	x	y	z	Occupation Factor
Ho	0	0	0	1
Y	0.5	0.5	0.5	0.5
Sb	0.5	0.5	0.5	0.5
O(1)	−0.173	0.125	0.125	1
O(2)	0.125	0.125	0.125	1

Table 2. Structural eigenvalues of Bi_2MoO_6 fabricated by solvothermal synthesis technique.

Atom	x	y	z	Occupation Factor
Bi(1)	0.517	0.426	0.983	0.383
Bi(2)	0.473	0.078	0.969	0.602
Mo	0.005	0.244	0.000	0.182
O(1)	0.057	0.140	0.076	0.850
O(2)	0.259	0.999	0.263	0.690
O(3)	0.240	0.500	0.255	0.400
O(4)	0.705	0.232	0.250	0.790
O(5)	0.213	0.263	0.330	0.960
O(6)	0.516	0.359	0.561	0.690

The observed distortions in the MO_6 octahedra (M = Y^{3+} and Sb^{5+}) of Ho_2YSbO_7 indicate a crystal structure distortion, which has been proven to enhance photocatalytic efficiency in previous studies [46]. Additionally, the unique crystal structure of Ho_2YSbO_7,

composed of interconnected MO_6 (M = Y^{3+} and Sb^{5+}) octahedra through Ho^{3+} ions, exhibits distinctive Ho-O bond distances and bond angles. In the crystal structure of Ho_2YSbO_7, there are two types of Ho–O bond lengths: the six longer Ho–O(1) bond lengths (4.766 Å) and the two shorter Ho–O(2) bond lengths (2.242 Å). The six M–O(1) (M = Y^{3+} and Sb^{5+}) bond lengths were determined as 1.988 Å, and the M–Ho (M = Y^{3+} and Sb^{5+}) bond length was 3.661 Å. The M–O–M (M = Y^{3+} and Sb^{5+}) bond angles were measured as 134.020°, while the Ho-M-Ho (M = Y^{3+} and Sb^{5+}) bond angles were 135.00° in the crystal structure of Ho_2YSbO_7. The Ho–M–O (M = Y^{3+} and Sb^{5+}) bond angles were found to be 137.431°. The M–O–M bond angles in Ho_2YSbO_7 could impact the mobility of PICs, thus influencing their ability to reach the surface reaction centers and affect the photocatalytic efficiency [46]. Moreover, the larger Ho–Y–O and Ho–Sb–O bond angles in Ho_2YSbO_7 may further enhance its photocatalytic properties.

The remarkable photocatalytic performance of Ho_2YsbO_7 could be attributed to its unique crystalline structure and electronic properties. The insights gained into the crystallographic and electronic characteristics of Ho_2YsbO_7 are crucial for understanding and optimizing its photocatalytic capabilities.

2.2. FTIR Analysis

To investigate the presence of functional groups and chemical bonds in HBHP, Ho_2YsbO_7, and Bi_2MoO_6, FTIR spectra were collected using an FTIR spectrometer, as shown in Figure 4. The bending vibrations of Ho-O were observed at 560 cm^{-1} [72,73]. The bending vibrations of Sb–O and Sb–O–Sb were detected at 619 cm^{-1} and 690 cm^{-1}, respectively [74,75]. The stretching vibrations of Y-O appeared at 713 cm^{-1} [76]. The bands observed at 847 cm^{-1} and 806 cm^{-1} could be assigned to the asymmetric and symmetric stretching modes of MoO_6, respectively, involving vibrations of the apical oxygen atoms [77]. The 748 cm^{-1} mode represented the asymmetric stretching mode of MoO_6, involving vibrations of the equatorial oxygen atoms. The bands observed at 578 cm^{-1} and 532 cm^{-1} correspond to the bending vibrations of MoO_6 [77]. Additionally, a small band at 474 cm^{-1} could be attributed to the stretching and bending vibrations of BiO_6 octahedra [77].
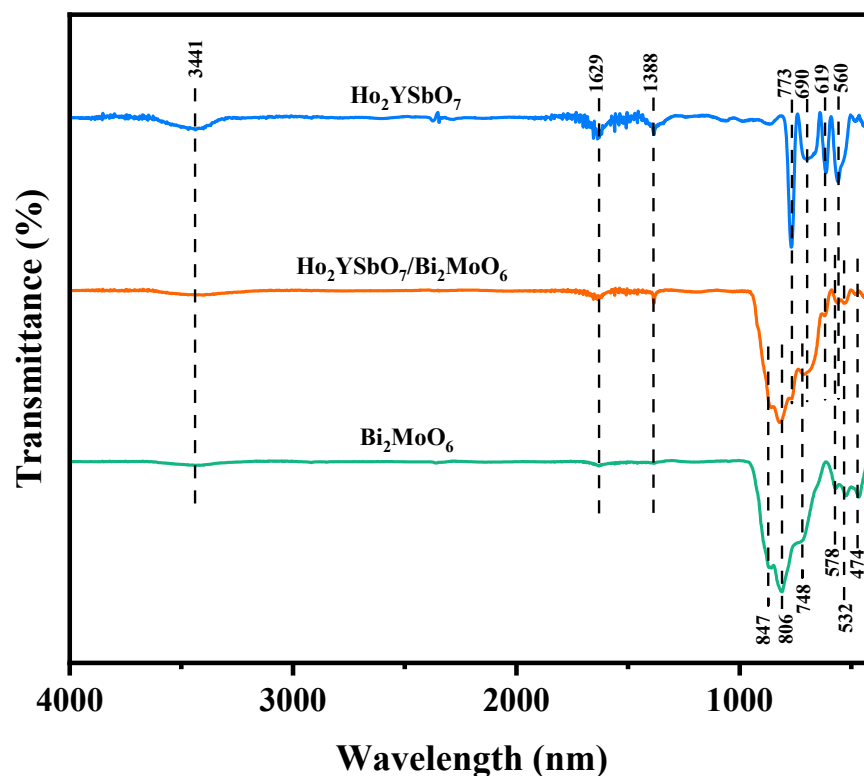

Figure 4. FTIR spectra of Ho_2YsbO_7, Bi_2MoO_6, and HBHP.

The broad bands centered around 3441 cm^{-1} were indicative of the stretching vibration mode of hydroxyl (OH) groups adsorbed with water [78]. Similarly, the absorption bands observed at 1629 cm^{-1} correspond to the bending vibration of surface OH groups [78]. Additionally, the peaks observed at 1388 cm^{-1} could be attributed to the vibrational mode of C-H bonds [78].

2.3. Raman Analysis

Raman spectroscopy was deployed to investigate the chemical bonding characteristics as well as the molecular vibrations and rotations of HBHP, Ho$_2$YSbO$_7$, and Bi$_2$MoO$_6$ in this study. Figure 5 illustrates the obtained Raman spectra for Ho$_2$YSbO$_7$, Bi$_2$MoO$_6$, and HBHP. The Raman spectra of Ho$_2$YSbO$_7$ exhibited several notable modes, such as the A$_1$-type stretching vibration of the Sb–O–Sb bond at 232 cm^{-1} and the A$_g$-type stretching vibration of the Ho–O bond at 382 cm^{-1} [79,80]. Additionally, the Y–O bond displayed an A$_g$ bending vibration mode at 458 cm^{-1} [81]. The presence of another peak at 710 cm^{-1} could be attributed to the Sb–O–Sb stretching with T$_2$ symmetry [79]. In case of Bi$_2$MoO$_6$, strong Raman modes observed at 283 cm^{-1} were associated with the E$_g$ bending vibrations. The modes at 304 cm^{-1} and 333 cm^{-1} were identified as the E$_u$ symmetric bending vibrations [77]. Moreover, the 714 cm^{-1} mode represented the asymmetric stretching vibration (E$_u$ mode) of the MoO$_6$ octahedra, involving the movement of equatorial oxygen atoms connecting the MoO$_6$ octahedra within the layers [77]. The Raman vibrations at 793 cm^{-1} and 832 cm^{-1} were, respectively, attributed to the A$_{1g}$ symmetric and A$_{2u}$ asymmetric stretching vibrations of the MoO$_6$ octahedra, involving the motion of apical oxygen atoms directed towards the (Bi$_2$O$_2$)$^{2+}$ layers [77,82,83]. These observed peaks confirm the presence of pure phases, consistent with the XRD results. The distinctive peaks in the Raman spectrum of HBHP at 232 cm^{-1}, 283 cm^{-1}, 304 cm^{-1}, 333 cm^{-1}, 382 cm^{-1}, 458 cm^{-1}, 714 cm^{-1}, 732 cm^{-1}, 793 cm^{-1}, and 832 cm^{-1} validate the unique characteristics of both Ho$_2$YSbO$_7$ and Bi$_2$MoO$_6$. These findings further support the successful integration of both materials within the heterostructure photocatalyst.
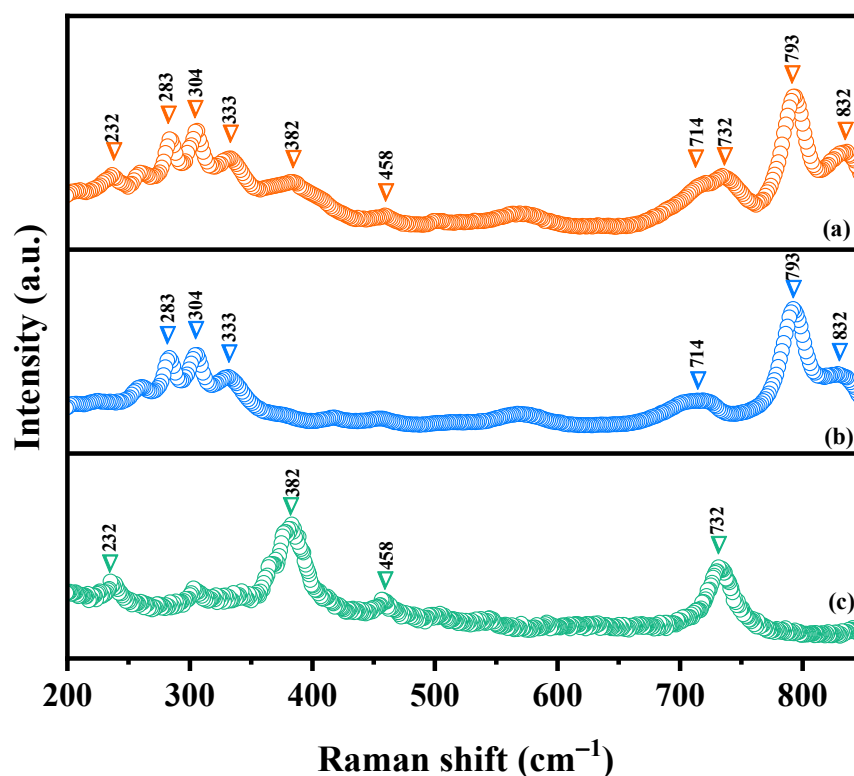

Figure 5. Raman spectra of (**a**) HBHP, (**b**) Bi$_2$MoO$_6$, and (**c**) Ho$_2$YSbO$_7$.

2.4. UV-Vis Diffuse Reflectance Spectra

To investigate the band structure of the synthesized samples, a detailed analysis of the absorption spectra of Ho_2YSbO_7, Bi_2MoO_6, and HBHP was conducted, as presented in Figure S2a. The absorption verges of the diffuse reflectance spectra of Ho_2YSbO_7 and Bi_2MoO_6 were observed at around 450 nm and 505 nm, respectively. Notably, HBHP exhibited a distinctive absorption verge at approximately 520 nm, demonstrating a significant red-shift compared to Ho_2YSbO_7 and Bi_2MoO_6. This observation suggests that HBHP possesses a higher light absorption capacity than either Ho_2YSbO_7 or Bi_2MoO_6.

To determine the energy difference between the bands in these samples, the Kubelka–Munk function (1) was employed [84,85]. This method involves identifying the cross-section point at which the photon energy ($h\nu$) axis intersects with the line extrapolated from the linear section of the absorption spectrum peaks. By utilizing this approach, the energy disparity between the bands in the samples could be assessed.

$$\frac{[1 - R_d(h\nu)]^2}{2R_d(h\nu)} = \frac{\alpha(h\nu)}{S} \tag{1}$$

In this given equation, the scattering index, the diffuse reflection, and the absorbance factor of radiation were assigned to S, R_d, and α, respectively.

The optical absorption characteristics close to the band verges of the samples cohered with the Equation (2) [86,87]:

$$(\alpha h\nu)^{\frac{1}{n}} = A(h\nu - E_g) \tag{2}$$

The given equation introduced in this study involves the symbols A, α, E_g, and ν, which, respectively, represent the relative factor, absorbance factor, band energy difference, and photon frequency. The parameter n is utilized to characterize the transition property of photoinduced electrons, with a value of 1/2 for direct transition and a value of 2 for indirect transition [88,89].

Analyzing the results presented in Figure S2b, the calculated band gap values for Ho_2YSbO_7 and Bi_2MoO_6 were determined as 2.686 eV and 2.483 eV, respectively. Both materials exhibited an n value close to 2, indicating indirect transition. Similarly, the band gap value for HBHP was computed as 2.387 eV, suggesting indirect transition. The significantly lower E_g value of HBHP compared to those of Ho_2YSbO_7 and Bi_2MoO_6 provides strong evidence of HBHP's superior light absorption capacity.

Similarly, Figure S3a presents the absorption spectra of NTO and pristine TiO_2. In the diffuse reflectance spectra of TiO_2, the absorption edge was observed at approximately 400 nm. Notably, NTO exhibited a distinct absorption edge at around 445 nm, indicating a significant red-shift compared to TiO_2. Moreover, Figure S3b enables the determination of the band gap values for NTO and TiO_2 as 2.781 eV and 3.064 eV, respectively. The considerably lower band gap value and the higher absorption edge observed in NTO compared to TiO_2 provide compelling evidence of its superior light absorption capacity within the visible light range, confirming the successful fabrication of NTO [67–69].

2.5. X-ray Photoelectron Spectroscopy Analysis

X-ray photoelectron spectroscopy (XPS) was utilized to evaluate the chemical makeup and oxidation states of HBHP, Ho_2YSbO_7, and Bi_2MoO_6. The survey spectrum in Figure S4 indicates the presence of Ho, Y, Sb, Bi, Mo, and O elements in HBHP, with the carbon peak serving as a calibration reference. When comparing the spectrum of Ho_2YSbO_7 with HBHP, distinct bismuth and molybdenum signals were observed in the latter, indicating the inclusion of Bi_2MoO_6 in HBHP.

Figure 6a,b display the spectral peaks of Ho $4d_{5/2}$, Y $3d_{5/2}$, Bi $4f_{7/2}$, Bi $4f_{5/2}$, Mo $3d_{5/2}$, and Mo $3d_{3/2}$ in Ho_2YSbO_7, Bi_2MoO_6, and HBHP. These peaks exhibited slight shifts towards higher binding energies in HBHP compared to the former compounds, indicating notable interfacial interactions between Ho_2YSbO_7 and Bi_2MoO_6 within the heterostructure. The spin–orbit separation values between Bi $4f_{7/2}$ and Bi $4f_{5/2}$ were 5.31 eV for both

Bi$_2$MoO$_6$ and HBHP, confirming the exclusive presence of Bi^{3+} [90]. Similarly, the spin–orbit separation values between Mo 3d$_{3/2}$ and Mo 3d$_{5/2}$ were 3.13 eV for both Bi$_2$MoO$_6$ and HBHP, indicating the exclusive presence of Mo^{6+} [91].
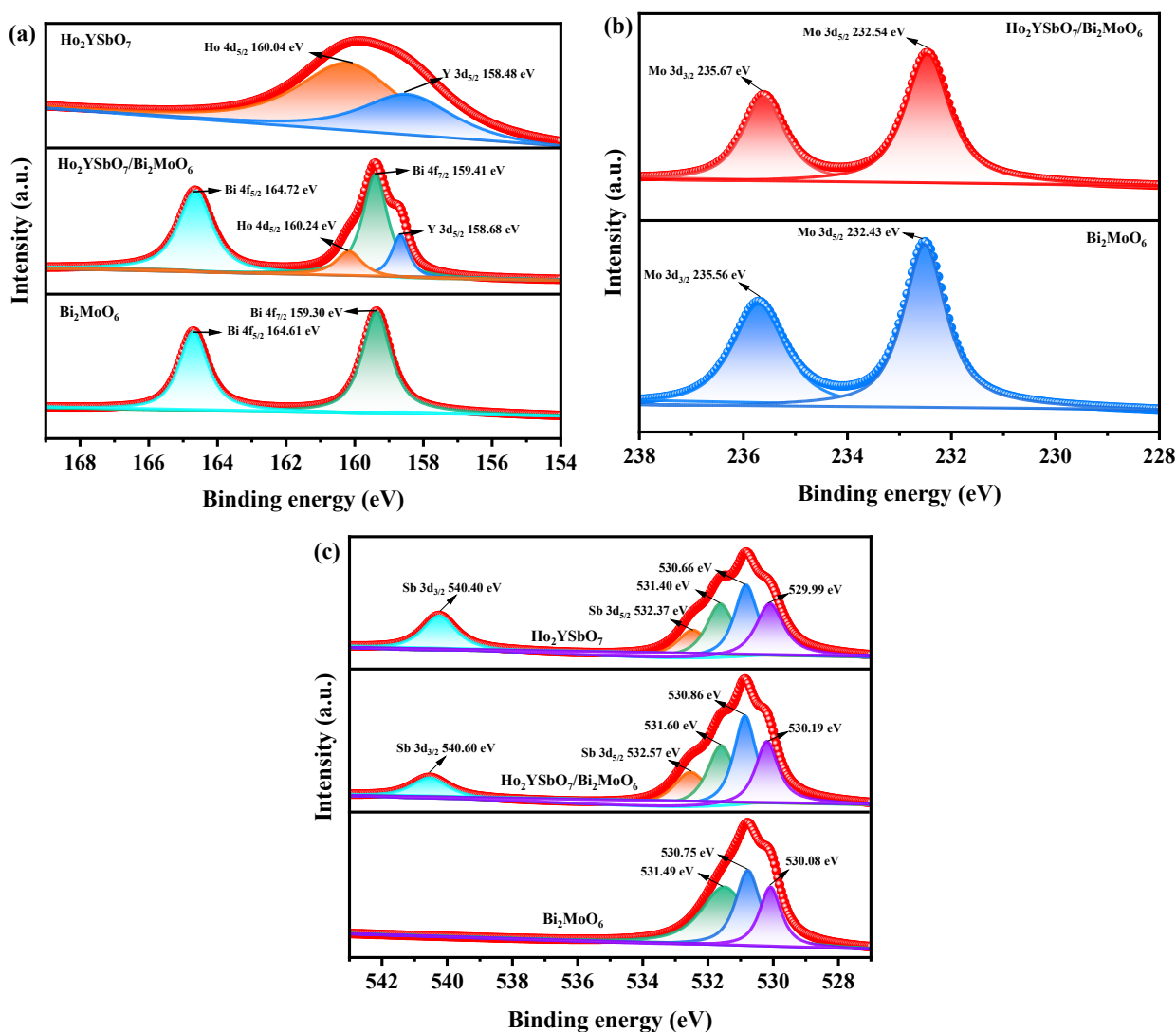

Figure 6. The corresponding high-resolution XPS spectra of (**a**) Ho 4d, Y 3d, and Bi 4f; (**b**) Mo 3d; (**c**) and O 1s and Sb 3d of HBHP, Ho$_2$YSbO$_7$, and Bi$_2$MoO$_6$.

Figure 6c showcases the deconvoluted O 1s spectrum of HBHP, Ho$_2$YSbO$_7$, and Bi$_2$MoO$_6$. The observed peaks at 530.19 eV, 529.99 eV, and 530.08 eV correspond to the lattice oxygen [92]. Furthermore, the peaks at 530.86 eV, 530.66 eV, and 530.75 eV signify the signal originating from hydroxyl groups [93]. Additionally, the peaks at 531.60 eV, 531.40 eV, and 531.49 eV correspond to the signal associated with oxygen vacancies [92,93]. Notably, in the case of HBHP, the location of the deconvoluted O 1s peaks manifested evident shifts in comparison to their positions in pure Ho$_2$YSbO$_7$ and Bi$_2$MoO$_6$ samples. These shifts provided further evidence of interfacial interactions between Ho$_2$YSbO$_7$ and Bi$_2$MoO$_6$ species. Moreover, the spin–orbit disassociation numerical value between Sb 3d$_{5/2}$ and Sb 3d$_{3/2}$ was consistently measured as 8.03 eV for both Ho$_2$YSbO$_7$ and HBHP, which confirms the exclusive presence of Sb^{5+} species [94].

Furthermore, Figure S5 presents the XPS survey spectrum of NTO. The spectrum revealed the presence of O, Ti, C, and N elements, indicating the successful incorporation of nitrogen in the TiO$_2$ [67–69]. These results, in conjunction with the XRD analysis, were consistent with previous findings and provide further evidence of the successful synthesis

of NTO [67–69]. Moreover, Figure S6a,b display the spectral peaks corresponding to Ti $2p_{3/2}$, Ti $2p_{1/2}$, and N 1s, respectively, while Figure S6c exhibits the deconvoluted O 1s spectrum of NTO [67–69]. The presence of peaks at 531.41 eV, 530.21 eV, and 529.91 eV could be attributed to oxygen vacancies, hydroxyl groups, and lattice oxygen, respectively [92,93].

Based on the XPS analysis, it has been determined that the oxidation states of Ho, Y, Sb, Bi, Mo, and O ions in the material are +3, +3, +5, +3, +6, and −2, respectively. This finding confirms the successful fabrication of the photocatalytic samples based on the ideational chemical formula. Moreover, the surface elemental analysis revealed an average atomic ratio of Ho/Y/Sb/Bi/Mo/O as 826:411:407:854:419:7083, indicating the atomic ratios of Ho/Y/Sb and Bi/Mo in the HBHP sample of 2.03:1.01:1.00 and 2.04:1.00, respectively. No additional phases were observed by analyzing the XPS peaks of Ho_2YSbO_7 and Bi_2MoO_6, confirming their absence.

2.6. TEM-EDS Analysis

The morphology and elemental composition of HBHP were investigated using transmission electron microscopy (TEM) and energy-dispersive X-ray spectroscopy (EDS). Figures 7 and 8 depict TEM images and EDS elemental mapping of HBHP, respectively, with Ho, Y, Sb, and O derived from Ho_2YSbO_7, and Bi, Mo, and O from Bi_2MoO_6. The EDS spectrum of HBHP is presented in Figure S7. The EDS element mapping analysis presented in Figure 8 provided compelling evidence for the presence of Ho, Y, Sb, Bi, Mo, and O elements within the HBHP, thereby supporting the coexistence of Ho_2YSbO_7 and Bi_2MoO_6. Furthermore, through a careful examination of the light-emitting zones associated with Ho, Y, and Sb in comparison to Bi and Mo, it could be deduced that the larger microboulders correspond to Ho_2YSbO_7, while the smaller microboulders correspond to Bi_2MoO_6. This observation was substantiated by the visual arrangement of larger Ho_2YSbO_7 particles enveloped by the smaller Bi_2MoO_6 microparticles, as evident in Figures 7 and 8. Consequently, these findings served as robust evidence validating the successful fabrication of the HBHP. Meanwhile, these findings were consistent with the XPS results depicted in Figures S4 and 6. Additionally, the EDS spectrum (Figure S7) revealed an atomic ratio of approximately 826:413:409:853:421:7078 for Ho/Y/Sb/Bi/Mo/O, which closely matched the atomic ratio obtained from the XPS analysis. Based on these comprehensive results, it could be convincingly concluded that HBHP was successfully fabricated with high purity under the employed preparation conditions.
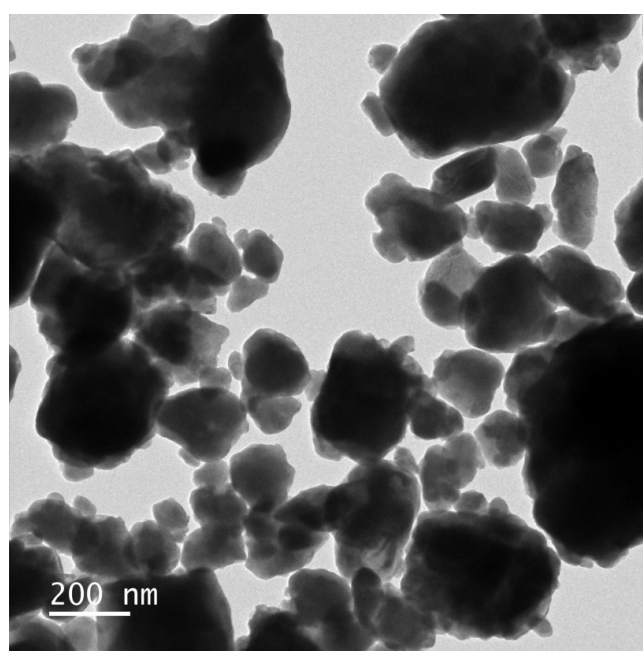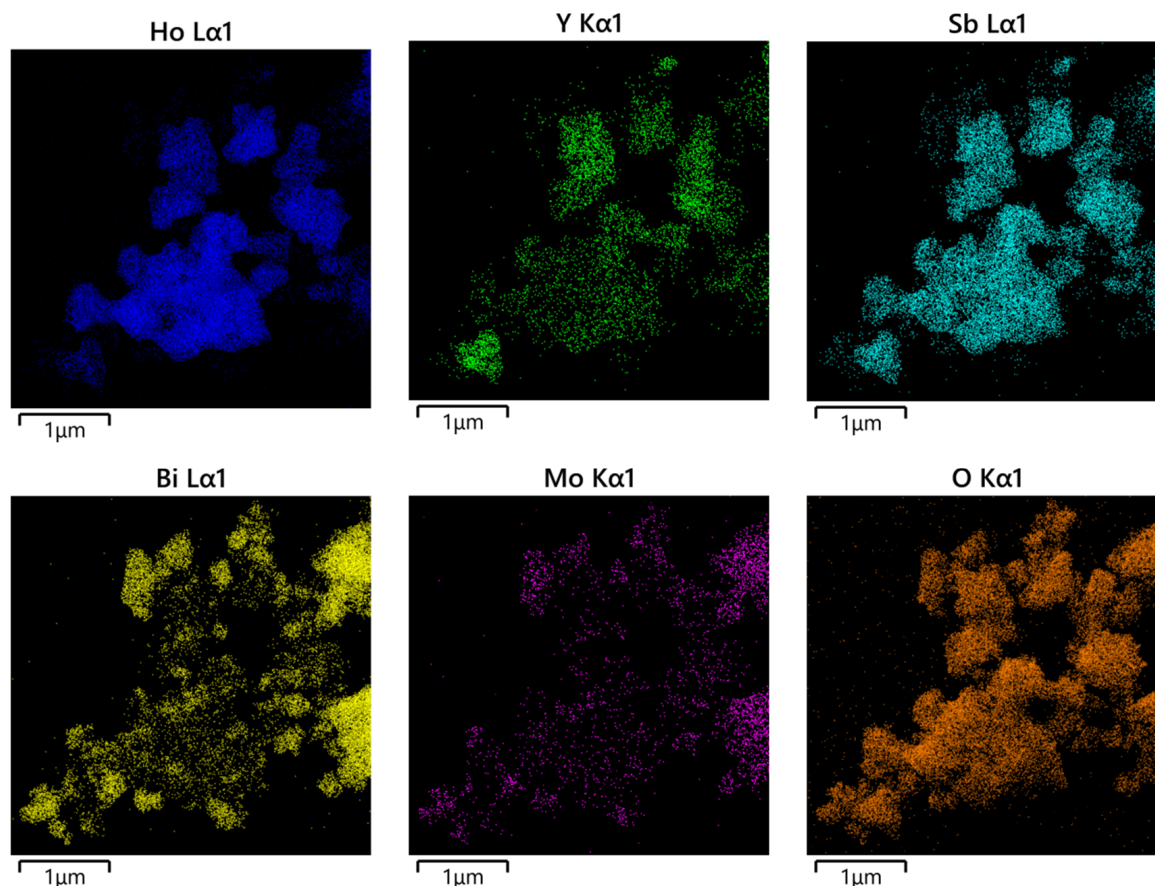

Figure 7. TEM image of HBHP.

Figure 8. EDS elemental mapping of HBHP (Ho, Y, Sb, and O from Ho_2YSbO_7 and Bi, Mo, and O from Bi_2MoO_6).

2.7. Photocatalytic Activity

Photocatalytic Activity in Photodegradation Experiments

The wastewater sample was collected from the Songhua River in Jilin Province, China. After pretreatment, the concentration of DRN in the wastewater was determined to be 0.032 mmol/L. The aim of this investigation was to assess the concentration variability profiles of DRN during the photodegradation process under VLE using a range of photocatalysts, including HBHP, Ho_2YSbO_7, Bi_2MoO_6, and NTO. NTO, a widely recognized visible-light-responsive photocatalyst, was employed as a benchmark to assess and compare the differences in photodegradation efficiency among various catalyst samples. As illustrated in Figure S8a, the experimental results clearly demonstrated a continuous decrease in DRN concentration during prolonged irradiation in the presence of the photocatalyst samples. This observation highlighted the effective degradation capability of the photocatalysts. In contrast, the photolysis assay results revealed no significant change in DRN concentration over the same extended period of irradiation in the absence of photocatalyst samples, confirming that the observed degradation could be attributed to the photocatalytic activity rather than mere photolysis.

To assess the REF of DRN, the equation $(1 - \frac{C}{C_0}) \times 100\%$ was utilized, with *C* representing the instantaneous saturation of DRN and C_0 representing the initial saturation of DRN. Upon analysis of the data from Figure S8a, it was observed that the use of HBHP as the photocatalyst resulted in a remarkable DRN REF of 99.78% within pesticide wastewater after 152 min of VLE, corresponding to a reaction velocity of 3.50×10^{-9} mol·L^{-1}·s^{-1} and a photonic efficiency (PEC) of 0.0735%. Similarly, when Ho_2YSbO_7 was employed as the photocatalyst, it showcased a conspicuous DRN REF of 88.44%, with a reaction velocity of 3.10×10^{-9} mol·L^{-1}·s^{-1} and a PEC of 0.0651%. Furthermore, the use of Bi_2MoO_6 as

the photocatalyst led to a pronounced DRN REF of 82.19%, accompanied by a reaction velocity of 2.88×10^{-9} mol·L^{-1}·s^{-1} and a PEC of 0.0605%. In comparison, NTO exhibited a DRN REF of 33.78%, with a reaction velocity of 1.18×10^{-9} mol·L^{-1}·s^{-1} and a photonic efficiency of 0.0248% [95,96].

These findings clearly indicate that HBHP demonstrated the highest photodegradation efficiency for DRN among the various photocatalysts studied. Additionally, the photodegradation efficiencies achieved with Ho_2YSbO_7 and Bi_2MoO_6 as photocatalysts also surpassed that of NTO. Furthermore, a comparison of the DRN degradation velocities after 152 min of VLE revealed the superior performance of HBHP, surpassing that of Ho_2YSbO_7 by 1.13 times, Bi_2MoO_6 by 1.21 times, and NTO by 2.95 times.

Figure S8b presents the saturation variation profiles of total organic carbon (TOC) throughout the photodegradation procedure of DRN in pesticide wastewater under VLE using different photocatalysts, including HBHP, Ho_2YSbO_7, Bi_2MoO_6, and NTO. The efficiency of the removal of TOC could be calculated by $(1 - \frac{TOC}{TOC_0}) \times 100\%$, where TOC represents the instantaneous saturation of total organic carbon and TOC_0 represents the initial saturation of total organic carbon. An analysis of Figure S8b revealed that following 152 min of VLE, the REF values of TOC within pesticide wastewater were 97.19%, 83.33%, 77.81%, and 28.68% when employing HBHP, Ho_2YSbO_7, Bi_2MoO_6, and NTO as photocatalysts, respectively, for the treatment of DRN [97,98]. Moreover, a comparison of the TOC mineralization effectiveness after 152 min of VLE revealed the superior performance of HBHP, surpassing that of Ho_2YSbO_7 by 1.17 times, Bi_2MoO_6 by 1.25 times, and NTO by 3.39 times.

In conclusion, the results unequivocally showcased HBHP's superior performance in terms of the REF for both DRN and TOC during the degradation process, outperforming Ho_2YsbO_7, Bi_2MoO_6, and NTO. Notably, the REF of TOC when utilizing Ho_2YSbO_7 significantly exceeded that of Bi_2MoO_6 or NTO. These findings underscore HBHP's exceptional capabilities in both the mineralization and degradation of DRN, positioning it as a highly effective photocatalyst, surpassing the performance of Ho_2YSbO_7, Bi_2MoO_6, and NTO.

The concentration fluctuation graphs of DRN and TOC during five consecutive degradation cycles utilizing HBHP as a photocatalyst under VLE are illustrated in Figure S9a,b respectively. Following 152 min of VLE, the REF values of DRN were recorded at 99.78%, 98.66%, 97.63%, 96.56%, and 95.66% across the five cycles. Similarly, the REF values of TOC were documented at 97.19%, 96.11%, 95.10%, 94.06%, and 93.13% over the same cycles. These observations underscore the exceptional stability of HBHP during the degradation process. Moreover, a marginal reduction of 4.12% in the DRN degradation rate and a minor decrease of 4.06% in the TOC REF were noted throughout five consecutive degradation cycles. These findings indicate the remarkable structural stability of HBHP and its potential for effective reuse as a photocatalyst.

Figure 9 presents the first-order kinetic plots of DRN (Figure 9a) and TOC (Figure 9b) during the photodegradation process of DRN using various photocatalysts (HBHP, Ho_2YSbO_7, Bi_2MoO_6, and NTO) under VLE. The kinetic constants were determined using the formulas $\left(ln\frac{C_0}{C} = k_C t\right)$ and $\left(ln\frac{TOC_0}{TOC} = k_{TOC} t\right)$, where C_0 and C represent the initial and reaction saturation of DRN, and TOC_0 and TOC represent the initial and reaction saturation of total organic carbon. The calculated k_C values from the dynamic DRN saturation versus light exposure time graphs were 0.0334 min^{-1}, 0.0115 min^{-1}, 0.0093 min^{-1}, and 0.0022 min^{-1} for HBHP, Ho_2YSbO_7, Bi_2MoO_6, and NTO, respectively. Similarly, the k_{TOC} values derived from the dynamic TOC saturation versus light exposure time curves were 0.0201 min^{-1}, 0.0098 min^{-1}, 0.0086 min^{-1}, and 0.0016 min^{-1} for HBHP, Ho_2YSbO_7, Bi_2MoO_6, and NTO, respectively. Crucially, it is noteworthy that the k_{TOC} values were consistently lower than the k_C values for all the catalysts, indicating the generation of photodegradation intermediates during the process. Notably, HBHP exhibited significantly higher mineralization efficiency for DRN degradation compared to the other catalysts.
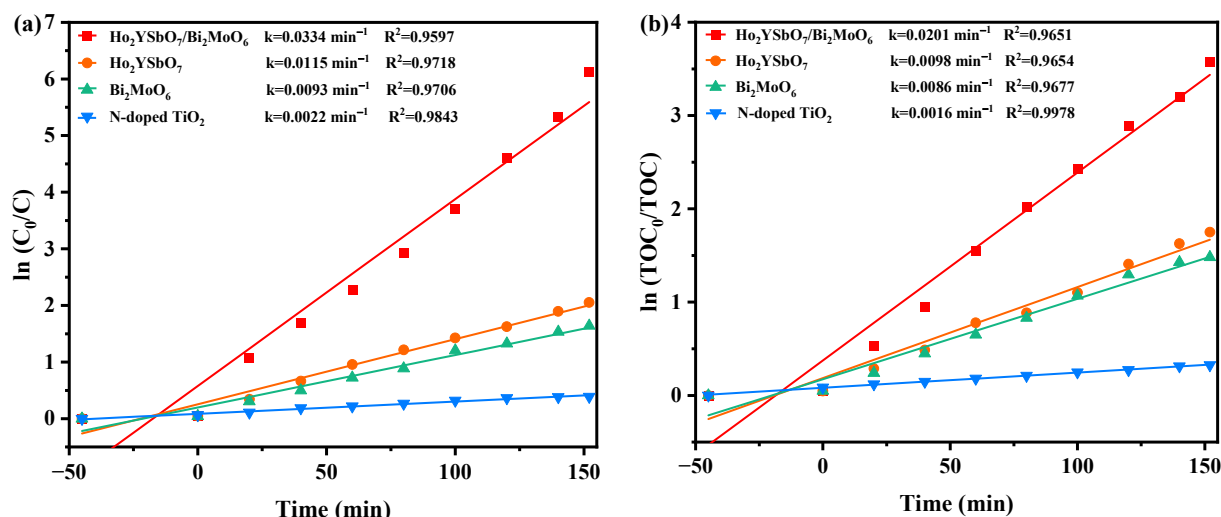
Figure 9. Observed first-order kinetics charts for (**a**) DRN and (**b**) TOC during photodegradation of DRN with HBHP, Ho_2YSbO_7, Bi_2MoO_5, or NTO as the catalytic sample under VLE.

Figure 10 displays the first-order kinetic plots of DRN and TOC during the photocatalytic degradation of DRN with HBHP, showcased in Figure 10a,b, respectively, under visible light conditions across five consecutive degradation cycles. The k_C values derived from the dynamic DRN saturation versus light exposure time curves with HBHP as the sample for the five cycles in Figure 10a were determined as 0.0334 min^{-1}, 0.0241 min^{-1}, 0.0215 min^{-1}, 0.0195 min^{-1}, and 0.0181 min^{-1}. Similarly, the k_{TOC} values obtained from the dynamic TOC saturation versus light exposure time curves with HBHP as the sample for the three cycles were measured as 0.0201 min^{-1}, 0.0192 min^{-1}, 0.0172 min^{-1}, 0.0158 min^{-1}, and 0.0151 min^{-1}. These findings validated the first-order reaction kinetics governing the photodegradation process of DRN in pesticide sewage using HBHP.
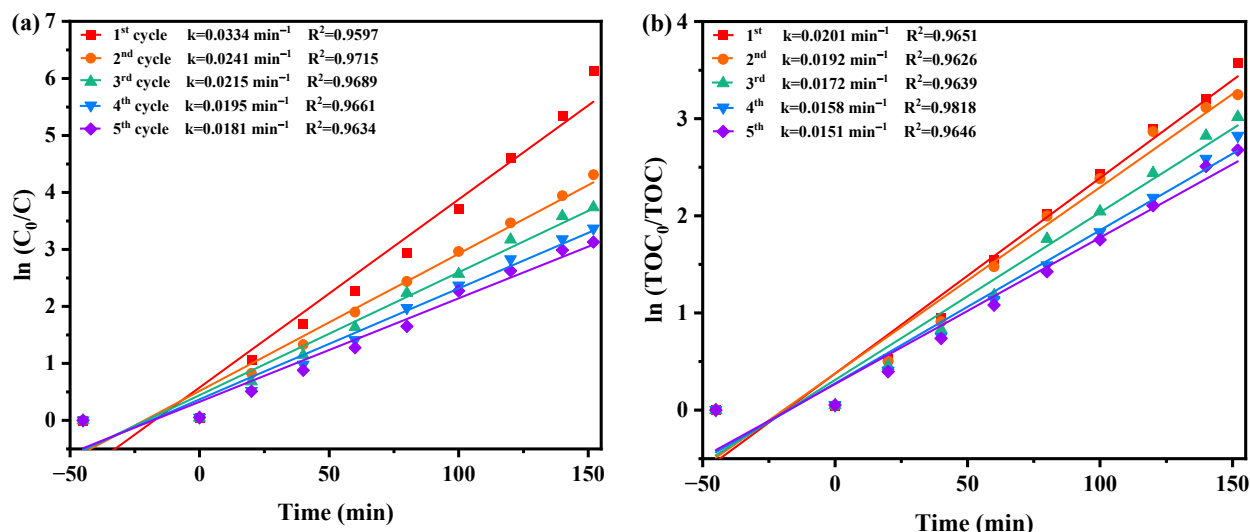

Figure 10. Observed first-order kinetic charts for (**a**) DRN and (**b**) TOC during photodegradation of DRN with HBHP as the catalytic sample under VLE for five cycle degradation tests.

2.8. Property Characterization

Figure 11a,b investigate the influence of benzoquinone (BQ), isopropanol (IPA), and ethylene diamine tetraacetic acid (EDTA) as radical scavengers on the REF of DRN using HBHP as the catalytic material under VLE. IPA was used to apprehend $\bullet OH$, BQ was employed to apprehend $\bullet O_2^-$, and EDTA was utilized to apprehend h^+. The scavengers

were added during the initial stage of the photodegradation process to determine the active species responsible for degradation. Compared to the control group, the presence of BQ reduced the average DRN REF by 46.03%, while IPA and EDTA resulted in reductions of 37.28% and 29.78%, respectively. These results indicated the involvement of $\bullet O_2^-$, $\bullet OH$, and h^+ as active radicals in the degradation process, with $\bullet O_2^-$ exhibiting the highest oxidation removal capability. Thus, when HBHP acted as the photocatalyst, $\bullet O_2^-$ radicals effectively eliminated DRN in pesticide-contaminated sewage. The ascending order of oxidation removal ability for degrading DRN was determined as $\bullet O_2^- > \bullet OH > h^+$.

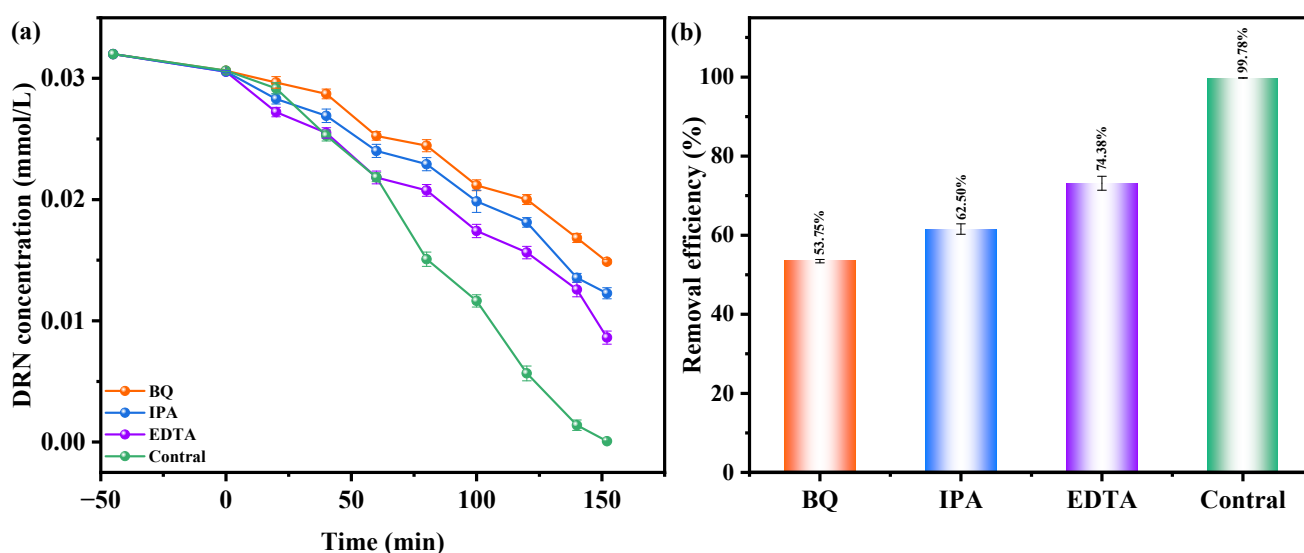**Figure 11.** Effect of different radical scavengers on (**a**) DRN saturation and (**b**) removal efficiency of DRN.

Electron paramagnetic resonance (EPR) analysis was conducted to investigate the generation of $\bullet O_2^-$ radicals and $\bullet OH$ radicals during the photodegradation process. The EPR spectrum in Figure 12 illustrates the signals for DMPO$\bullet O_2^-$ and DMPO$\bullet OH$ when HBHP was utilized as the photocatalyst. Following a 10 min exposure to visible light, the EPR spectrum exhibited a distinctive DMPO$\bullet O_2^-$ signal with four strong peaks in an equal intensity ratio of 1:1:1:1, confirming the presence of $\bullet O_2^-$ radicals [99]. Subsequently, the EPR spectrum displayed a four-line signal with a 1:2:2:1 intensity ratio, denoting the DMPO$\bullet OH$ signal acquired after VLE [99]. These observations implied the simultaneous generation of $\bullet O_2^-$ radicals and $\bullet OH$ radicals during the photodegradation process. Notably, the relative intensity of the EPR signals indicates a higher yield of $\bullet O_2^-$ radicals compared to $\bullet OH$ radicals [99,100]. These findings support the results obtained from the previous radical-scavenger experiments, further substantiating the involvement of $\bullet O_2^-$ radicals and $\bullet OH$ radicals in the degradation mechanism.

To investigate the interfacial carriers' optical properties, the dynamical behavior of the electronic excited states, and the lifetime, multiple measurement methodologies were employed. Figure S10a–d display the photoluminescence (PL) spectrum and time-Resolved photoluminescence (TRPL) spectra of Ho_2YSbO_7, Bi_2MoO_6, and HBHP. The PL spectrum was obtained using an excitation wavelength of 300 nm with a scan speed of 1200 nm/min. Higher PL intensities typically indicate faster recombination rates of the PIC, resulting in a lower photocatalytic effect [101,102]. In Figure S10a, HBHP exhibits the lowest radiative intensity, suggesting efficient charge separation and constrained recombination of the PIC. Ho_2YSbO_7 displayed a higher radiative intensity compared to HBHP, while Bi_2MoO_6 exhibited the highest radiative intensity among all three samples. These findings demonstrated that the heterostructure sample enhanced the photocatalytic efficiency towards DRN. Moreover, additional evidence was provided to support the superior photocatalytic performance

of HBHP compared to Ho_2YSbO_7 and Bi_2MoO_6. The TRPL spectra in Figure S10b–d were fitted using a double-exponential decay equation (Equation (3)) [103]:

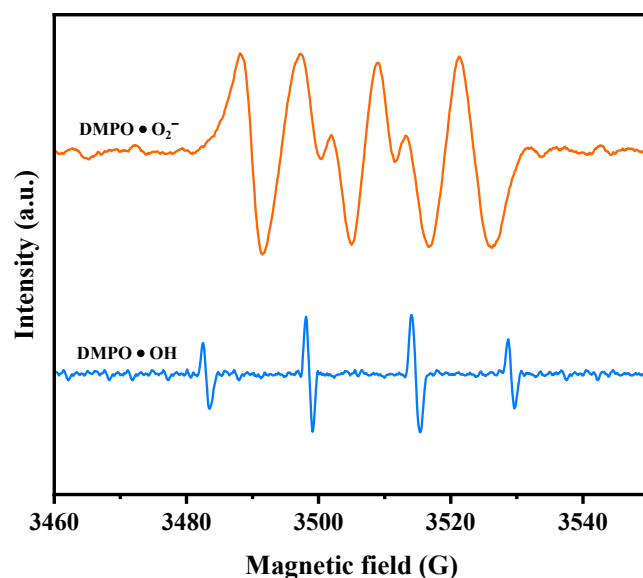$$I(t) = I_0 + A_1\exp\left(-\frac{t}{\tau_1}\right) + A_2\exp\left(-\frac{t}{\tau_2}\right) \tag{3}$$

Figure 12. EPR spectrum for DMPO·O_2^- and DMPO·OH over HBHP.

According to the presented equation, the first- and second-order decay times, A_1 and A_2, are weighting coefficients of each decay channel [104]. To determine the average PIC lifetime (τ_{ave}), Equation (4) was utilized [105]:

$$\tau_{ave} = \left(A_1\tau_1^2 + A_2\tau_2^2\right)/(A_1\tau_1 + A_2\tau_2) \tag{4}$$

The calculated lifetimes and corresponding parameters are presented in Table S1. HBHP exhibited significantly longer lifetimes ($\tau_1 = 1.4139$ ns, $\tau_2 = 130.9981$ ns, $\tau_{ave} = 99.7314$ ns) compared to Ho_2YSbO_7 ($\tau_1 = 1.2890$ ns, $\tau_2 = 116.1575$ ns, $\tau_{ave} = 85.3321$ ns) and Bi_2MoO_6 ($\tau_1 = 1.0946$ ns, $\tau_2 = 11.6284$ ns, $\tau_{ave} = 5.7917$ ns). These results unequivocally establish the unparalleled superiority of HBHP in terms of photocatalytic efficacy, surpassing that of the individual components Ho_2YSbO_7 and Bi_2MoO_6.

The influence of prepared HBHP, Ho_2YSbO_7, and Bi_2MoO_6 samples on the efficiency of electron–hole pair separation was investigated through photocurrent (PC) and electrochemical impedance spectroscopy (EIS) experiments. In Figure 13a, the transient photocurrent responses of HBHP, Ho_2YSbO_7, and Bi_2MoO_6 samples clearly demonstrated that HBHP exhibited the highest photocurrent response. This could be attributed to the efficient diffusion of photoexcited electrons, while the photoexcited holes rapidly transfer to the surface of Bi_2MoO_6 due to the electric potential difference of the valence band between Ho_2YSbO_7 and Bi_2MoO_6 within the HBHP [106]. The increased photocurrent response in HBHP indicated effective separation of the PIC and its prolonged lifetime during the photocatalytic degradation reaction [107]. Likewise, results from the EIS experiments in Figure 13b support this finding, with the relative arc sizes in the EIS Nyquist plot for the three electrodes following the order HBHP < Ho_2YSbO_7 < Bi_2MoO_6, confirming that HBHP exhibited the highest efficiency in charge separation [108,109]. The PC and EIS results underscored that the construction of a heterojunction significantly mitigated the recombination of electron–hole pairs and promoted the efficient separation of photogenerated charges compared with individual samples. These findings were consistent with the PL and TRPL analyses, further highlighting the exceptional photocatalytic efficacy achieved with HBHP.
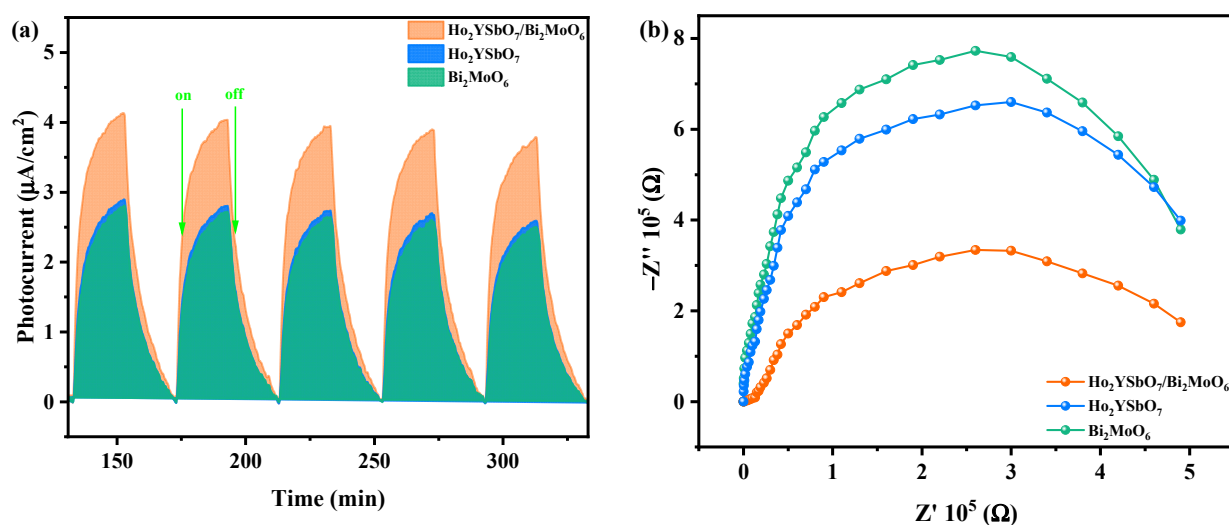
Figure 13. (**a**) Transient photocurrent and (**b**) Nyquist impedance plots of HBHP, Ho_2YSbO_7, and Bi_2MoO_6.

2.9. Analysis of Possible Degradation Mechanisms

Figure 14 exhibits the UPS spectra of Ho_2YSbO_7 and Bi_2MoO_6, while Figure 15 illustrates the proposed photocatalytic degradation mechanism of DRN with HBHP as the catalytic sample under VLE. The UPS analysis aimed to precisely determine the ionization potential of Ho_2YSbO_7 and Bi_2MoO_6, with the onset (Ei) and cutoff (Ecutoff) binding energies for both samples shown in Figure 14 [110]. The measured values were 1.360 eV and 19.754 eV for Ho_2YSbO_7, and 0.674 eV and 20.136 eV for Bi_2MoO_6 [111]. Based on the excitation energy (approximately 21.2 eV), the ionization potential of Ho_2YSbO_7 and Bi_2MoO_6 was determined as 2.806 eV and 1.738 eV, respectively [112]. Consequently, the conduction band (CB) potential of Ho_2YSbO_7 and Bi_2MoO_6 was estimated as 0.120 eV and −0.745 eV, respectively.
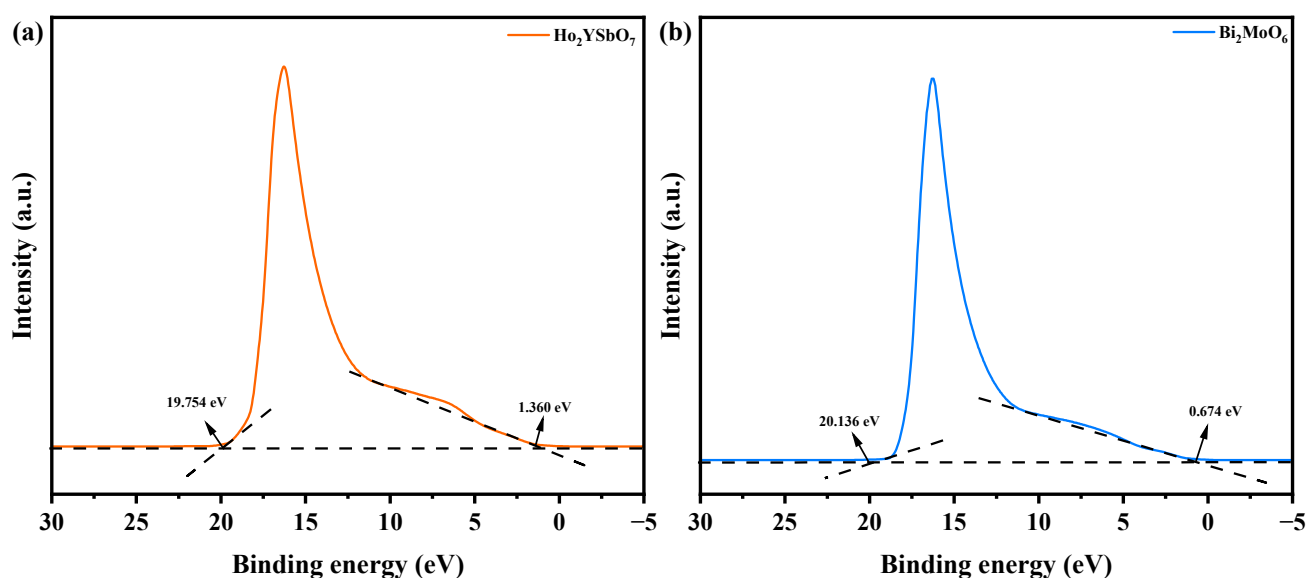

Figure 14. UPS spectra of (**a**) Ho_2YSbO_7 and (**b**) Bi_2MoO_6 (the intersections of the black dash lines indicated by the black arrows indicated the onset (Ei) and cutoff (Ecutoff) binding energy).
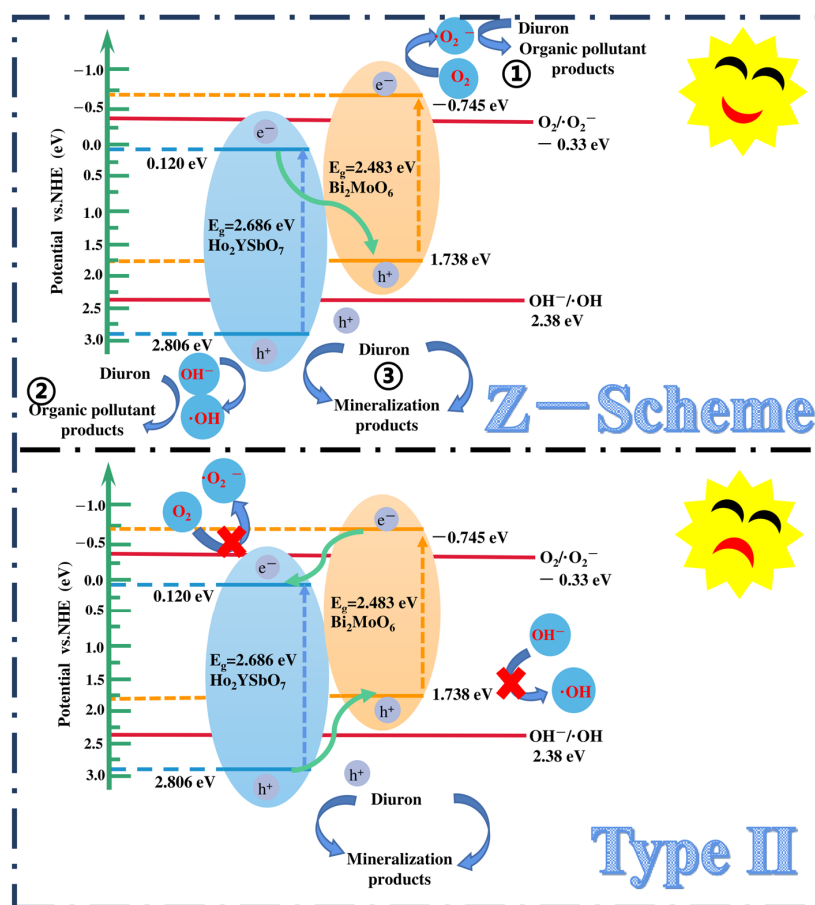
Figure 15. Possible photodegradation mechanism of DRN with HBHP as photocatalyst under VLE.

Based on the comprehensive and prominent analysis of the various heterojunctions proposed by Barrocas et al. [113] and the above analysis of the CB and VB positions of Ho_2YSbO_7 and Bi_2MoO_6, two potential photocatalytic mechanisms, namely the conventional type-II and direct Z-scheme heterojunction, could be considered to explain the enhanced transfer of PICs in this study, as illustrated in Figure 15. In the conventional type-II heterostructure, the photoexcited electrons and holes, generated at the CB (-0.745 eV) of Bi_2MoO_6 and VB (2.806 eV) of Ho_2YSbO_7, respectively, readily migrated to the CB (0.120 eV) of Ho_2YSbO_7 and the VB (1.738 eV) of Bi_2MoO_6. This migration was facilitated by the potential difference at the heterojunction. However, this migration resulted in a reduction in the redox potential of the photoinduced carriers. Moreover, the more positive CB edge of Ho_2YSbO_7 (0.120 eV) compared to the reduction potential of $O_2/\bullet O_2^-$ (-0.33 eV vs. NHE) [114] and the more negative VB edge of Bi_2MoO_6 relative to the oxidation potential of $OH^-/\bullet OH$ (2.38 eV vs. NHE) made the formation of $\bullet O_2^-$ and $\bullet OH$ species unfavorable [115,116]. Notably, these findings contradicted the results obtained from the active radical trapping experiment and EPR measurement, as demonstrated in Figures 11 and 12. In light of these contradictory results, it was postulated that the direct Z-scheme heterojunction may provide a more appropriate explanation for the photocatalytic mechanism observed in the Ho_2YSbO_7/Bi_2MoO_6 heterojunction.

In the proposed Z-scheme mechanism in Figure 15, the photogenerated electrons were expected to migrate from the CB (0.120 eV) of Ho_2YSbO_7 to the VB (1.738 eV) of Bi_2MoO_6. This migration lead to the effective separation of PICs and the maintenance of higher reduction/oxidation potentials during photocatalytic reactions. Moreover, the electrons located in the CB (-0.745 eV) of Bi_2MoO_6 could react with O_2, forming $\bullet O_2^-$ species, which were responsible for the decomposition of DRN (① in Figure 15). Similarly, the electrons presented in the VB (2.806 eV) of Ho_2YSbO_7 could react with OH^-, producing $\bullet OH$ species

that participated in the decomposition of DRN (② in Figure 15). Furthermore, the photoinduced holes in the VB of Bi_2MoO_6 or Ho_2YSbO_7 could directly catalyze the oxidation and subsequent degradation of DRN due to its inherent strong oxidation capability (③ in Figure 15). Importantly, this analysis was consistent with the experimental results obtained through the active radical trapping experiment and EPR measurement, as demonstrated in Figures 11 and 12. Therefore, it could be concluded that under VLE, the PIC migration pathway within the heterojunction composed of Ho_2YSbO_7 and Bi_2MoO_6 followed the direct Z-scheme. The significantly enhanced photocatalytic performance of the HBHP was closely associated with the successful construction of the direct Z-scheme heterojunction.

The photocatalytic degradation system of DRN was investigated, and the intermediate products formed during the process were analyzed utilizing a liquid chromatograph–mass spectrometer (LC-MS). By referring to the previous literature, five main intermediates were identified, contributing to a comprehensive understanding of the degradation pathway of DRN [117,118]. A mechanistic scheme illustrating this pathway is depicted in Figure 16. Table S2 presents the identification of five intermediate products based on their respective molecular ions and mass fragment ions. The table also includes information such as the retention time (Rt), molecular weight (M.W.), and characteristic ions of these identified products. The degradation process commenced with •OH attacking specific sites on diuron, namely the methyl groups and the aromatic ring. Notably, this initial step did not involve dechlorination or alkyl chain modifications but led to the formation of four primary photoproducts: P1 ($C_5H_5Cl_2N$, $m/z = 162$) [117], P2 ($C_8H_{11}Cl_2N_2O_2$, $m/z = 248$) [117], 1-(3,4-dichlorophenyl)-3-methylurea (DCPMU, $C_8H_8Cl_2N_2O$, $m/z = 219$) [117], and 3,4-dichlorophenylurea (DCPU, $C_7H_6Cl_2N_2O$, $m/z = 205$) [118,119]. Subsequently, oxidation processes ensued, resulting in the elimination of alkyl groups and chlorine atoms. These reactions ultimately yielded the photoproduct P3 (C_6H_6ClNO, $m/z = 143$) [117,118]. In addition to these five compounds, other degradation products could still possibly exist in the photocatalytic system but were not detected because of their low concentration, extraction efficiency, and limited sensitivity in LC/MS. Many researchers have identified other degradation products during photocatalytic processes by HPLC, 1H NMR, and GC/MS, as well as these five products [117,119–121]. Finally, the oxidative opening of the aromatic ring occurred, generating the final products: Cl^-, NO_3^-, NH_4^+, CO_2, and H_2O.
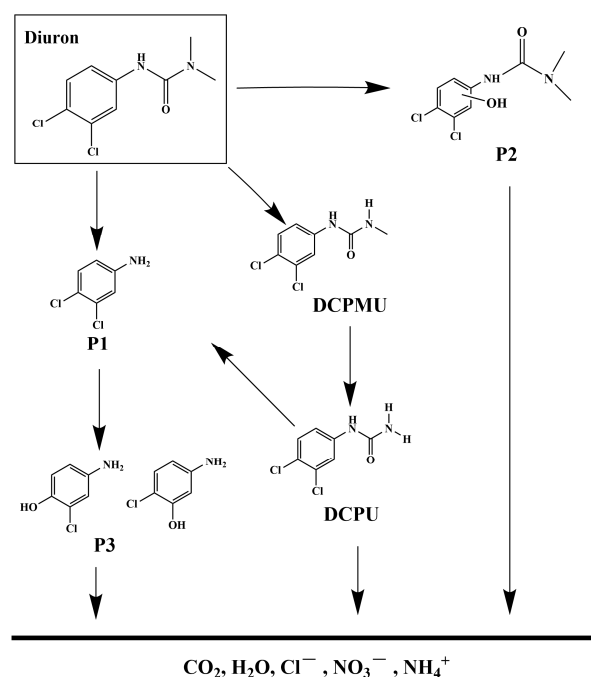

Figure 16. Suggested photodegradation pathway scheme for DRN under visible light condition with HBHP as photocatalytic sample.

3. Experimental Section

3.1. Materials and Reagents

$Ho(NO_3)_3 \cdot 5H_2O$ (purity = 99.99%), $Y(NO_3)_3 \cdot 6H_2O$ (purity = 99.9%), and $SbCl_5$ (purity = 99.999%) were procured from Shanghai Macklin Biochemical Co., Ltd. (Shanghai, China). $Bi(NO_3)_3 \cdot 5H_2O$ (purity = 99.99%) and Na_2MoO_4 (purity = 99.9%) were obtained from Aladdin Group Chemical Reagent Co., Ltd. (Shanghai, China). Additionally, ethylene-diaminetetraacetic acid (EDTA, $C_{10}H_{16}N_2O_8$, purity = 99.99%) and P-benzoquinone (BQ, $C_6H_4O_2$, purity $\geq$ 99.0%) were acquired from Shanghai Macklin Biochemical Co., Ltd. (Shanghai, China). Isopropyl alcohol (IPA, C_3H_8O, purity $\geq$ 99.999%) was purchased from Aladdin Group Chemical Reagent Co., Ltd. (Shanghai, China). Furthermore, pure ethanol (C_2H_5OH, purity $\geq$ 99.5%) and DRN ($C_9H_{10}Cl_2N_2O$, purity $\geq$ 99.5%) were carefully selected and deemed suitable for gas chromatography, meeting the specifications set by the American Chemical Society. Both of the chemicals were acquired from Shanghai Macklin Biochemical Co., Ltd. (Shanghai, China).

3.2. Preparation Method of Bi_2MoO_6

The Bi_2MoO_6 catalyst was prepared via the solvothermal method in this study. First, equal volumes of $Bi(NO_3)_3 \cdot 5H_2O$ (0.30 mol/L) and Na_2MoO_4 (0.15 mol/L) precursor solutions were meticulously mixed and stirred for 1200 min. Subsequently, the resulting precursor mixture was transferred into a high-pressure autoclave equipped with a polytetrafluoroethylene (PTFE) liner, followed by maintaining it at a temperature of 210 °C for 900 min. Next, the mixture was subjected to a controlled heating process in a tube furnace under a nitrogen (N_2) atmosphere with a heating rate of 7.0 °C/min until it reached 750 °C. The mixture was then held at this temperature for 480 min. Consequently, pure Bi_2MoO_6 powder was successfully synthesized.

3.3. Preparation Method of Ho_2YSbO_7

The Ho_2YSbO_7 catalyst was prepared via the solvothermal method in this study. Firstly, equal volumes of $Ho(NO_3)_3 \cdot 5H_2O$ (0.30 mol/L), $Y(NO_3)_3 \cdot 6H_2O$ (0.15 mol/L), and $SbCl_5$ (0.15 mol/L) precursor solutions were thoroughly mixed and stirred for a duration of 1500 min. Subsequently, the precursor mixture was transferred into a high-pressure autoclave equipped with a PTFE liner and maintained at a temperature of 220 °C for 800 min. Next, the resulting mixture was heated under a N_2 atmosphere utilizing a tube furnace at a heating rate of 7.5 °C/min until reaching a temperature of 800 °C, and held at this temperature for 500 min. Finally, pure Ho_2YSbO_7 powder was successfully synthesized.

3.4. Synthesis of N-Doped TiO_2

The sol–gel synthesis process was employed to fabricate NTO. Initially, a certain amount of butyl titanate was mixed with anhydrous ethanol to prepare solution M. Concurrently, glacial acetic acid, di-distilled water, and anhydrous ethanol were mixed to form solution N. Subsequently, solution M was added dropwise to solution N under magnetic stirring. After the complete addition, the mixture was stirred for an additional 30 min, resulting in a translucent gel-like suspension. Next, nitrogen doping was conducted by immersing the gel in urea to achieve a N/Ti mole ratio of 8 mol%. The suspension was stirred for an additional 60 min. Subsequently, the gel was air-dried at room temperature for 40 h, leading to the formation of a solid gel. The dried gel was crushed and subjected to calcination at 500 °C for 3.5 h. Finally, the NTO catalyst was obtained using a vibrating screen and utilized for subsequent investigation.

3.5. Synthesis of Ho_2YSbO_7/Bi_2MoO_6 Heterojunction Photocatalyst

HBHP was prepared by the hydrothermal method. First, equal volumes of $Ho(NO_3)_3 \cdot 5H_2O$ (3 mol/L), $Y(NO_3)_3 \cdot 6H_2O$ (1.5 mol/L), and $SbCl_5$ (1.5 mol/L) were thoroughly mixed. The resulting solution was then transferred into a high-pressure reaction vessel lined with PTFE. The reaction medium consisted of a glycerol–water solution, with polyethylene glycol or

ethylene glycol added as a dispersant. The solution volume occupied 60% of the high-pressure vessel. The high-pressure vessel was placed inside a high-temperature sintering furnace and heated to 240 °C while maintaining a pressure of 150 MPa for 1200 min. After the furnace cooled down to room temperature, the powder was extracted and subjected to centrifugal filtration. The resulting powder was washed three times with acetone, deionized water, and pure ethanol before being dried in a vacuum oven at 50 °C for 3 h. Subsequently, the dried powder mixture was compressed into thin slices and sintered in a high-temperature furnace. The heating process began at 20 °C and gradually increased to 950 °C over a duration of 100 min. The temperature was subsequently maintained at 950 °C for 600 min before cooling down with the furnace. Finally, pure Ho_2YSbO_7 powder was obtained.

Similarly, equal volumes of $Bi(NO_3)_3 \cdot 5H_2O$ (3 mol/L) and Na_2MoO_4 (1.5 mol/L) were thoroughly mixed. The resulting solution was transferred into a high-pressure reaction vessel lined with PTFE, using the same reaction medium and dispersant as mentioned before. The volume of the solution occupied 60% of the high-pressure vessel. The high-pressure vessel was placed inside a high-temperature sintering furnace and heated to 200 °C while maintaining a pressure of 90 MPa for 1080 min. After cooling to room temperature, the powder was extracted and subjected to centrifugal filtration. The resulting powder was washed three times with acetone, deionized water, and pure ethanol before being dried in a vacuum oven at 50 °C for 3 h. Subsequently, the dried powder mixture was pressed into thin pellets and sintered in a high-temperature furnace. The heating process began at 20 °C and gradually increased to 850 °C over a duration of 90 min. The temperature was then maintained at 850 °C for 400 min before cooling down with the furnace. The sintered pellets were crushed into powder, resulting in the successful synthesis of pure Bi_2MoO_6.

Finally, a mixture of 1 mol of Ho_2YSbO_7 and 1 mol of Bi_2MoO_6 in 300 mL of octanol ($C_8H_{18}O$) was subjected to 60 min of ultrasonic treatment in an ultrasonic bath. The mixture was then rapidly stirred under reflux conditions at 150 °C for 150 min to facilitate the adhesion of Bi_2MoO_6 onto the surface of Ho_2YSbO_7 nanoparticles, forming Ho_2YSbO_7/Bi_2MoO_6 heterojunction photocatalytic materials. After cooling to room temperature, the product was obtained through centrifugation and washed three times with a mixture of n-hexane and ethanol. The purified powder was dried in a vacuum oven at 50 °C for 5 h and stored in a desiccator for further use. Ultimately, Ho_2YSbO_7/Bi_2MoO_6 heterojunction photocatalytic materials were successfully fabricated.

3.6. Characterization

The pure-phase Ho_2YSbO_7 and Bi_2MoO_6 samples, synthesized via the hydrothermal synthesis technique, were characterized using a comprehensive array of advanced analytical techniques. These include X-ray diffractometry (XRD), UV-Vis diffuse reflectance spectrophotometry (UV-Vis DRS), Fourier transform infrared spectroscopy (FTIR), Raman spectroscopy, X-ray photoelectron spectroscopy (XPS), transmission electron microscopy (TEM), energy dispersive X-ray spectroscopy (EDS), ultraviolet photoelectron spectroscopy (UPS), a fluorescence spectrophotometer, and electron paramagnetic resonance (EPR) spectroscopy. XRD analysis was performed using an X-ray diffractometer (XRD-6000, Shimadzu Corporation, Kyoto, Japan) to obtain crystallographic information. Microstructural and morphological features were examined using transmission electron microscopy (TEM, JEM—F200 FEI Tecnai G2 F20 FEI Talos F200s), and the elemental composition was determined through energy-dispersive spectroscopy (EDS). UV-Vis diffuse reflectance spectrophotometry (UV-Vis DRS, UV-3600, Shimadzu Corporation, Kyoto, Japan) was employed to study the optical properties of the samples. Functional groups and chemical bonds were analyzed using a Fourier infrared spectrometer (FTIR, WQF-530A, Beifen-Ruili Analytical Instrument (Group) Co., Ltd., Beijing, China). Raman spectrometry (INVIA0919-06, RENISHAW plx, Wotton-under-Edge, Gloucestershire, GL12 8JR, London, UK) was employed to investigate chemical bond interactions. The surface chemical composition and states were examined using X-ray photoelectron spectroscopy (XPS, PHI 5000 VersaProbe, UlVAC-PHI,

Maoqi City, Japan). Ultraviolet photoelectron spectroscopy (UPS, Escalab 250 xi, Thermo Fisher Scientific, Waltham, MA, USA) was utilized to measure the ionization potential of the valence band. The related information about the free radicals in the samples was detected using an electron paramagnetic resonance spectrometer (EPR, A300, Bruker Corporation, Karlsruhe, Germany). The properties of PICs were determined using a fluorescence spectrophotometer (FLS980, Edinburgh Instruments Ltd., Edinburgh, UK).

3.7. Photoelectrochemical Experiments

The electrochemical impedance spectroscopy (EIS) tests were performed using a CHI660D electrochemical workstation (Chenhua Instruments Co., Ltd., Shanghai, China) with a standard three-electrode setup. The working electrode consisted of the as-fabricated materials, while a platinum plate served as the counter electrode. A Ag/AgCl electrode was used as the reference electrode. A 0.5 mol/L Na_2SO_4 aqueous solution was used as the electrolyte. During the experiment, light simulation was carried out using a 500 W Xe lamp equipped with a 420 nm cutoff filter.

3.8. Experimental Setup and Procedure

The degradation experiments were conducted using a photocatalytic reactor (CEL-LB70, China Education Au-Light Technology Co., Ltd., Beijing, China). The visible light condition was simulated by a 500 W xenon lamp and a 420 nm cutoff filter.

In each experiment, 12 quartz tubes were used and each quartz tube was filled with a reaction solution with a volume of 40 mL. For chemical industry wastewater, the total reaction volume was 480 mL. The dosage of nanophase materials (Ho_2YSbO_7, Bi_2MoO_6, or HBHP) in each experiment was maintained at 0.5 g/L. The initial concentration of DRN in the solution was 0.025 mmol/L.

During the reaction, 3 mL samples of the dispersed system were periodically collected for analysis. After 152 min of light exposure, a 13 mL sample of the dispersed system was collected to measure the residual DRN concentration. The photocatalyst was then removed by filtration using a 0.22 μm PES (polyether sulfone) filter membrane. The remaining DRN concentration was determined using Agilent 200 high-performance liquid chromatography (Agilent Technologies, Palo Alto, CA, USA). In the post-photodegradation process of the DRN dispersion system, a volume of 10 μL was injected at a flow rate of 1 mL/min.

To establish adsorption/desorption equilibrium between the photocatalytic sample, DRN, and atmospheric oxygen, the dispersed system containing the sample and DRN was stirred in darkness for 45 min prior to light exposure. During light exposure, the dispersed system was stirred at a speed of 600 rpm.

The mineralization of DRN in the dispersed system was assessed using a TOC analyzer (TOC-5000 A, Shimadzu Corporation, Kyoto, Japan). In order to calibrate the TOC saturation during the DRN photocatalytic process, either potassium acid phthalate ($KHC_8H_4O_4$) or anhydrous sodium carbonate was utilized as the reference reactant. Calibration standards were prepared by using potassium acid phthalate with known carbon concentrations ranging from 0 to 100 mg/L. TOC saturation was evaluated across six samples, with each containing a reaction solution volume of 40 mL.

For the calibration experiments of intermediate reactants, liquid chromatography–mass spectrometry (LC-MS, Thermo Quest LCQ Duo, Thermo Fisher Scientific Corporation, Waltham, MA, USA) was employed. A Beta Basic-C18 HPLC column (150 mm × 2.1 mm, 5 μm ID, Thermo Fisher Scientific Corporation, Waltham, MA, USA) was used during the DRN photocatalytic process. After the photocatalytic reaction, a 20 μL solution resulting from the reaction was injected into the LC-MS system automatically. The system employed a mobile phase consisting of a mixture of 60% methanol and 40% ultrapure water. The mobile phase flowed through the system at a rate of 0.2 mL/min. The spray voltage was adjusted to 4800V, while maintaining the capillary temperature at 27 °C and the voltage at 19.00 V. For analysis, the mass-to-charge ratio (*m/z*) range was configured from 50 to 500.

In order to evaluate the photon intensity of the irradiating light, a 420 nm filter was utilized to select the desired range of radiation within the visible light spectrum. The calculation of the number of photons passing through the filter per unit time, whether total photons or reactive photons, could be performed using the formula $\upsilon = c/\lambda$. In this equation, υ represents the frequency of photons, λ corresponds to the wavelength of incident light, and c denotes the speed of light. By utilizing the precise numerical values of the Avogadro constant (NA) and Planck constant (h), the energy of a photon (hν) could be accurately determined. The irradiation photon flux could be adjusted by varying the distance between the photoreactor and the light source. To measure the incident photon flux, I_o, a radiometer (Model FZ-A, Photoelectric Instrument Factory Beijing Normal University, Beijing, China) was employed. The determined numerical value under light exposure was 4.76×10^{-6} Einstein L^{-1} s^{-1}. The PEC was determined with Equation (5):

$$\phi = R/I_o \tag{5}$$

where ϕ is the PEC (%), R is the retrogradation velocity of DRN (mol L^{-1} s^{-1}), and I_o is the irradiation photon flux (Einstein L^{-1} s^{-1}).

4. Conclusions

A groundbreaking Ho_2YSbO_7 photocatalyst was successfully synthesized using the solvothermal synthesis technique, while HBHP was synthesized through the hydrothermal fabrication technique. Characterization of the synthesized samples involved a comprehensive suite of techniques, including X-ray diffraction (XRD), ultraviolet–visible diffuse reflectance spectroscopy (UV-Vis DRS), Fourier transform infrared (FTIR) spectroscopy, Raman spectroscopy, X-ray photoelectron spectroscopy (XPS), transmission electron microscopy (TEM), energy-dispersive X-ray spectroscopy (EDS), a photocurrent (PC) test, electrochemical impedance spectroscopy (EIS), ultraviolet photoelectron spectroscopy (UPS), photoluminescence (PL) spectroscopy, and electron paramagnetic resonance (EPR) spectroscopy. The formation of the heterostructure between Ho_2YSbO_7 and Bi_2MoO_6 played a crucial role in enhancing the photocatalytic efficiency for pollutant degradation. Notably, HBHP exhibited outstanding removal performance for DRN in wastewater, achieving a remarkable REF of up to 99.78% for DRN and 97.19% for TOC within a short exposure time of 152 min. Comparative analysis demonstrated that HBHP displayed a significantly higher REF for DRN compared to the Ho_2YSbO_7, Bi_2MoO_6, and NTO photocatalysts, with the REF being 1.13 times, 1.25 times, and 2.95 times higher, respectively. The superior photocatalytic activity of HBHP could be attributed to its efficient separation and low recombination of PICs. The formation of the heterojunction between Ho_2YSbO_7 and Bi_2MoO_6 facilitated effective charge migration and the generation of free radicals, thus enhancing the degradation of DRN. This study identified $\bullet O_2{}^-$ radicals as the primary reactive species responsible for the degradation of DRN, with $\bullet OH$ and h^+ radicals also participating in the degradation process. Additionally, a plausible degradation pathway and mechanism for DRN were proposed. These findings offer promising strategies for the treatment of DRN-contaminated wastewater and are of great significance for the advancement of photocatalytic technology and the development of highly efficient nanophase photocatalytic materials for environmental pollutant degradation.

Author Contributions: Conceptualization, L.H. and J.L.; methodology, L.H. and J.L.; software, L.H. and J.L.; validation, L.H. and J.L.; formal analysis, L.H. and J.L.; investigation, L.H. and J.L.; resources, L.H. and J.L.; data curation, L.H. and J.L.; writing—original draft preparation, L.H. and J.L.; writing—review and editing, L.H. and J.L.; visualization, L.H. and J.L.; supervision, L.H. and J.L.; project administration, J.L.; funding acquisition, J.L. All authors have read and agreed to the published version of the manuscript.

Institutional Review Board Statement: Not applicable.

Informed Consent Statement: Not applicable.

Data Availability Statement: Data are contained within the article.

Conflicts of Interest: The authors declare no conflicts of interest.

References

1. Zeshan, M.; Bhatti, I.A.; Mohsin, M.; Iqbal, M.; Amjed, N.; Nisar, J.; AlMasoud, N.; Alomar, T.S. Remediation of pesticides using TiO$_2$ based photocatalytic strategies: A review. *Chemosphere* **2022**, *300*, 134525. [CrossRef]
2. Koe, W.S.; Lee, J.W.; Chong, W.C.; Pang, Y.L.; Sim, L.C. An overview of photocatalytic degradation: Photocatalysts, mechanisms, and development of photocatalytic membrane. *Environ. Sci. Pollut. Res.* **2020**, *27*, 2522–2565. [CrossRef]
3. Boruah, P.K.; Das, M.R. Dual responsive magnetic Fe$_3$O$_4$-TiO$_2$/graphene nanocomposite as an artificial nanozyme for the colorimetric detection and photodegradation of pesticide in an aqueous medium. *J. Hazard. Mater.* **2020**, *385*, 121516. [CrossRef]
4. Lopes, J.Q.; Cardeal, R.A.; Araújo, R.D.; Assunçao, J.C.D.; Salgado, B.C.B. Application of titanium dioxide as photocatalyst in diuron degradation: Operational variables evaluation and mechanistic study. *Eng. Sanit. Ambient.* **2021**, *26*, 61–68. [CrossRef]
5. Anirudhan, T.S.; Christa, J.; Shainy, F. Magnetic titanium dioxide embedded molecularly imprinted polymer nanocomposite for the degradation of diuron under visible light. *React. Funct. Polym.* **2020**, *152*, 104597. [CrossRef]
6. Eissa, F.; Zidan, N.E.H.; Sakugawa, H. Photodegradation of the herbicide diuron in water under simulated sunlight. *Geochem. J.* **2015**, *49*, 309–318. [CrossRef]
7. Mohammed, A.M.; Karttunen, V.; Huuskonen, P.; Huovinen, M.; Auriola, S.; Vähäkangas, K. Transplacental transfer and metabolism of diuron in human placenta. *Toxicol. Lett.* **2018**, *295*, 307–313. [CrossRef]
8. Fava, R.M.; Cardoso, A.P.F.; da Rocha, M.S.; Pontes, M.; de Camargo, J.L.V.; de Oliveira, M. Evaluation of early changes induced by diuron in the rat urinary bladder using different processing methods for scanning electron microscopy. *Toxicology* **2015**, *333*, 100–106. [CrossRef]
9. Khongthon, W.; Jovanovic, G.; Yokochi, A.; Sangvanich, P.; Pavarajarn, V. Degradation of diuron via an electrochemical advanced oxidation process in a microscale-based reactor. *Chem. Eng. J.* **2016**, *292*, 298–307. [CrossRef]
10. Liu, T.; Xu, S.; Lu, S.; Qin, P.; Bi, B.; Ding, H.; Liu, Y.; Guo, X.; Liu, X. A review on removal of organophosphorus pesticides in constructed wetland: Performance, mechanism and influencing factors. *Sci. Total Environ.* **2019**, *651 Pt 2*, 2247–2268. [CrossRef]
11. Matus, P.; Littera, P.; Farkas, B.; Urik, M. Review on Performance of Aspergillus and Penicillium Species in Biodegradation of Organochlorine and Organophosphorus Pesticides. *Microorganisms* **2023**, *11*, 1485. [CrossRef]
12. Burrows, H.D.; Canle, M.; Santaballa, J.A.; Steenken, S. Reaction pathways and mechanisms of photodegradation of pesticides. *J. Photochem. Photobiol. B-Biol.* **2002**, *67*, 71–108. [CrossRef]
13. Bouteh, E.; Ahmadi, N.; Abbasi, M.; Torabian, A.; van Loosdrecht, M.C.M.; Ducoste, J. Biodegradation of organophosphorus pesticides in moving bed biofilm reactors: Analysis of microbial community and biodegradation pathways. *J. Hazard. Mater.* **2021**, *408*, 124950. [CrossRef]
14. Zhao, G.; Huang, Q.Y.; Rong, X.M.; Cai, P.; Liang, W.; Dai, K. Biodegradation of methyl parathion in the presence of goethite: The effect of Pseudomonas sp Z1 adhesion. *Int. Biodeterior. Biodegrad.* **2014**, *86*, 294–299. [CrossRef]
15. Yang, Q.; Wang, J.; Zhang, W.; Liu, F.; Yue, X.; Liu, Y.; Yang, M.; Li, Z.; Wang, J. Interface engineering of metal organic framework on graphene oxide with enhanced adsorption capacity for organophosphorus pesticide. *Chem. Eng. J.* **2017**, *313*, 19–26. [CrossRef]
16. Sun, P.-F.; Liu, Y.; Mo, F.; Wu, M.X.; Xiao, Y.P.; Xiao, X.N.; Wang, W.; Dong, X.P. Efficient photocatalytic degradation of high-concentration moxifloxacin over dodecyl benzene sulfonate modified graphitic carbon nitride: Enhanced photogenerated charge separation and pollutant enrichment. *J. Clean. Prod.* **2023**, *393*, 136320. [CrossRef]
17. Barrocas, B.T.; Osawa, R.; Oliveira, M.C.; Monteiro, O.C. Enhancing Removal of Pollutants by Combining Photocatalysis and Photo-Fenton Using Co, Fe-Doped Titanate Nanowires. *Materials* **2023**, *16*, 2051. [CrossRef]
18. Barrocas, B.T.; Oliveira, M.C.; Nogueira, H.I.S.; Fateixa, S.; Monteiro, O.C. Ruthenium-Modified Titanate Nanowires for the Photocatalytic Oxidative Removal of Organic Pollutants from Water. *ACS Appl. Nano Mater.* **2019**, *2*, 1341–1349. [CrossRef]
19. Barrocas, B.; Oliveira, M.C.; Nogueira, H.I.S.; Fateixa, S.; Monteiro, O.C. A comparative study on emergent pollutants photo-assisted degradation using ruthenium modified titanate nanotubes and nanowires as catalysts. *J. Environ. Sci.* **2020**, *92*, 38–51. [CrossRef]
20. Arun, J.; Nachiappan, S.; Rangarajan, G.; Alagappan, R.P.; Gopinath, K.P.; Lichtfouse, E. Synthesis and application of titanium dioxide photocatalysis for energy, decontamination and viral disinfection: A review. *Environ. Chem. Lett.* **2023**, *21*, 339–362. [CrossRef]
21. Ali, H.M.; Roghabadi, F.A.; Ahmadi, V. Solid-supported photocatalysts for wastewater treatment: Supports contribution in the photocatalysis process. *Sol. Energy* **2023**, *255*, 99–125. [CrossRef]
22. Mehrjouei, M.; Müller, S.; Möller, D. A review on photocatalytic ozonation used for the treatment of water and wastewater. *Chem. Eng. J.* **2015**, *263*, 209–219. [CrossRef]

23. Zuraimi, M.S.; Magee, R.J.; Won, D.Y.; Nong, G.; Arsenault, C.D.; Yang, W.; So, S.; Nilsson, G.; Abebe, L.; Alliston, C. Performance of sorption- and photocatalytic oxidation-based indoor passive panel technologies. *Build. Environ.* **2018**, *135*, 85–93. [CrossRef]

24. Chong, M.N.; Jin, B.; Chow, C.W.K.; Saint, C. Recent developments in photocatalytic water treatment technology: A review. *Water Res.* **2010**, *44*, 2997–3027. [CrossRef] [PubMed]

25. Fernandes, S.M.; Barrocas, B.T.; Nardeli, J.V.; Montemor, M.F.; Maçoas, E.; Oliveira, M.C.; Oliveira, N.; de Carvalho, C.; Lauria, A.; Niederberger, M.; et al. Maximizing photocatalytic efficiency with minimal amount of gold: Solar-driven TiO$_2$ photocatalysis supported by MICROSCAFS® for facile catalyst recovery. *J. Environ. Chem. Eng.* **2024**, *12*, 112043. [CrossRef]

26. Kanakaraju, D.; Chandrasekaran, A. Recent advances in TiO$_2$/ZnS-based binary and ternary photocatalysts for the degradation of organic pollutants. *Sci. Total Environ.* **2023**, *868*, 161525. [CrossRef] [PubMed]

27. Yang, T.; Peng, J.; Zheng, Y.; He, X.; Hou, Y.; Wu, L.; Fu, X. Enhanced photocatalytic ozonation degradation of organic pollutants by ZnO modified TiO$_2$ nanocomposites. *Appl. Catal. B* **2018**, *221*, 223–234. [CrossRef]

28. Li, Z.; Sun, Y.; Xing, J.; Xing, Y.; Meng, A. One step synthesis of Co/Cr-codoped ZnO nanoparticle with superb adsorption properties for various anionic organic pollutants and its regeneration. *J. Hazard. Mater.* **2018**, *352*, 204–214. [CrossRef]

29. Ani, I.J.; Akpan, U.G.; Olutoye, M.A.; Hameed, B.H. Photocatalytic degradation of pollutants in petroleum refinery wastewater by TiO$_2$ and ZnO-based photocatalysts: Recent development. *J. Clean. Prod.* **2018**, *205*, 930–954. [CrossRef]

30. Nakata, K.; Fujishima, A. TiO$_2$ photocatalysis: Design and applications. *J. Photochem. Photobiol. C* **2012**, *13*, 169–189. [CrossRef]

31. He, Y.M.; Zhang, L.H.; Fan, M.H.; Wang, X.X.; Walbridge, M.L.; Nong, Q.Y.; Wu, Y.; Zhao, L.H. Z-scheme SnO$_{2-x}$/g-C$_3$N$_4$ composite as an efficient photocatalyst for dye degradation and photocatalytic CO$_2$ reduction. *Sol. Energy Mater. Sol. Cells* **2015**, *137*, 175–184. [CrossRef]

32. Marschall, R. Semiconductor Composites: Strategies for Enhancing Charge Carrier Separation to Improve Photocatalytic Activity. *Adv. Funct. Mater.* **2014**, *24*, 2421–2440. [CrossRef]

33. Zhao, C.R.; Cai, L.Y.; Wang, K.Q.; Li, B.X.; Yuan, S.D.; Zeng, Z.H.; Zhao, L.H.; Wu, Y.; He, Y.M. Novel Bi$_2$WO$_6$/ZnSnO$_3$ heterojunction for the ultrasonic-vibration-driven piezocatalytic degradation of RhB. *Environ. Pollut.* **2023**, *319*, 120982. [CrossRef] [PubMed]

34. Jiang, X.N.; Chen, S.; Zhang, X.R.; Qu, L.N.; Qi, H.J.; Wang, B.; Xu, B.B.; Huang, Z.H. Carbon-doped flower-like Bi$_2$WO$_6$ decorated carbon nanosphere nanocomposites with enhanced visible light photocatalytic degradation of tetracycline. *Adv. Compos. Hybrid Mater.* **2023**, *6*, 47. [CrossRef]

35. Shen, Z.Y.; Zhou, H.Y.; Pan, Z.C.; Guo, Y.; Yuan, Y.; Yao, G.; Lai, B. Degradation of atrazine by Bi$_2$MoO$_6$ activated peroxymonosulfate under visible light irradiation. *J. Hazard. Mater.* **2020**, *400*, 123187. [CrossRef] [PubMed]

36. Di, J.; Zhao, X.X.; Lian, C.; Ji, M.X.; Xia, J.X.; Xiong, J.; Zhou, W.; Cao, X.Z.; She, Y.B.; Liu, H.L.; et al. Atomically-thin Bi$_2$MoO$_6$ nanosheets with vacancy pairs for improved photocatalytic CO$_2$ reduction. *Nano Energy* **2019**, *61*, 54–59. [CrossRef]

37. Zhang, P.; Lu, X.F.; Luan, D.Y.; Lou, X.W. Fabrication of Heterostructured Fe$_2$TiO$_5$-TiO$_2$ Nanocages with Enhanced Photoelectrochemical Performance for Solar Energy Conversion. *Angew. Chem. Int. Ed.* **2020**, *59*, 8128–8132. [CrossRef]

38. Li, J.H.; Han, M.S.; Guo, Y.; Wang, F.; Sun, C. Fabrication of FeVO$_4$/Fe$_2$TiO$_5$ composite catalyst and photocatalytic removal of norfloxacin. *Chem. Eng. J.* **2016**, *298*, 300–308. [CrossRef]

39. Luan, J.F.; Li, Y.Y. Photocatalytic Water Splitting for Hydrogen Production with Gd$_2$MSbO$_7$ (M = Fe, In, Y) Photocatalysts under Visible Light Irradiation. *Materials* **2015**, *8*, 16–30. [CrossRef]

40. Devi, V.R.; Ravi, G.; Velchuri, R.; Muniratnam, N.R.; Prasad, G.; Vithal, M. Preparation, Characterization, Photocatalytic Activity and Conductivity Studies of YLnTi$_2$O$_7$(Ln = Nd, Sm, Eu and Gd). *Trans. Indian Ceram. Soc.* **2013**, *72*, 241–251. [CrossRef]

41. Zhang, H.S.; Liao, S.R.; Dang, X.D.; Guan, S.K.; Zhang, Z. Preparation and thermal conductivities of Gd$_2$Ce$_2$O$_7$ and (Gd$_{0.9}$Ca$_{0.1}$)$_2$Ce$_2$O$_{6.9}$ ceramics for thermal barrier coatings. *J. Alloys Compd.* **2011**, *509*, 1226–1230. [CrossRef]

42. Bi, J.; Wu, L.; Li, J.; Li, Z.; Wang, X.; Fu, X. Simple solvothermal routes to synthesize nanocrystalline Bi$_2$MoO$_6$ photocatalysts with different morphologies. *Acta Mater.* **2007**, *55*, 4699–4705. [CrossRef]

43. Liu, X.; Gu, S.; Zhao, Y.; Zhou, G.; Li, W. BiVO$_4$, Bi$_2$WO$_6$ and Bi$_2$MoO$_6$ photocatalysis: A brief review. *J. Mater. Sci. Technol.* **2020**, *56*, 45–68. [CrossRef]

44. Zhao, J.; Lu, Q.; Wei, M.; Wang, C. Synthesis of one-dimensional α-Fe$_2$O$_3$/Bi$_2$MoO$_6$ heterostructures by electrospinning process with enhanced photocatalytic activity. *J. Alloys Compd.* **2015**, *646*, 417–424. [CrossRef]

45. Li, J.; Liu, X.; Sun, Z.; Sun, Y.; Pan, L. Novel yolk–shell structure bismuth-rich bismuth molybdate microspheres for enhanced visible light photocatalysis. *J. Colloid Interface Sci.* **2015**, *452*, 109–115. [CrossRef]

46. Wang, J.H.; Zou, Z.G.; Ye, J.H. Synthesis, structure and photocatalytic property of a new hydrogen evolving photocatalyst Bi$_2$InTaO$_7$. In *Functionally Graded Materials VII: Proceedings of the 7th International Symposium on Functionally Grade Materials (FGM2002), Beijing, China, 15–18 October 2002*; Pan, W., Gong, J., Zhang, L., Chen, L., Eds.; Trans Tech Publications Ltd.: Bäch, Switzerland, 2003; Volume 423–424, pp. 485–490.

47. Barrocas, B.; Serio, S.; Rovisco, A.; Nunes, Y.; Jorge, M.E.M. Removal of rhodamine 6G dye contaminant by visible light driven immobilized Ca$_{1-x}$Ln$_x$MnO$_3$ (Ln = Sm, Ho; $0.1 \leq x \leq 0.4$) photocatalysts. *Appl. Surf. Sci.* **2016**, *360*, 798–806. [CrossRef]

48. Entradas, T.J.; Cabrita, J.F.; Barrocas, B.; Nunes, M.R.; Silvestre, A.J.; Monteiro, O.C. Synthesis of titanate nanofibers co-sensitized with ZnS and Bi$_2$S$_3$ nanocrystallites and their application on pollutants removal. *Mater. Res. Bull.* **2015**, *72*, 20–28. [CrossRef]

49. Barrocas, B.; Sério, S.; Rovisco, A.; Jorge, M.E.M. Visible-Light Photocatalysis in Ca$_{0.6}$H$_{0.4}$MnO$_3$ Films Deposited by RF-Magnetron Sputtering Using Nanosized Powder Compacted Target. *J. Phys. Chem. C* **2014**, *118*, 590–597. [CrossRef]

50. Cai, H.S.; Liu, G.G.; Lü, W.Y.; Li, X.X.; Yu, L.; Li, D.G. Effect of Ho-doping on photocatalytic activity of nanosized TiO_2 catalyst. *J. Rare Earths* **2008**, *26*, 71–75. [CrossRef]

51. Kulak, A.; Kokorin, A. Enhanced Titania Photocatalyst on Magnesium Oxide Support Doped with Molybdenum. *Catalysts* **2023**, *13*, 454. [CrossRef]

52. Jiang, J.Z.; Kato, K.; Fujimori, H.; Yamakata, A.; Sakata, Y. Investigation on the highly active $SrTiO_3$ photocatalyst toward overall H_2O splitting by doping Na ion. *J. Catal.* **2020**, *390*, 81–89. [CrossRef]

53. Song, K.X.; Zhang, C.; Zhang, Y.; Yu, G.L.; Zhang, M.J.; Zhang, Y.Y.; Qiao, L.; Liu, M.S.; Yin, N.; Zhao, Y.; et al. Efficient tetracycline degradation under visible light irradiation using $CuBi_2O_4/ZnFe_2O_4$ type II heterojunction photocatalyst based on two spinel oxides. *J. Photochem. Photobiol. A* **2022**, *433*, 114122. [CrossRef]

54. Zhu, B.C.; Cheng, B.; Fan, J.J.; Ho, W.K.; Yu, J.G. g-C_3N_4-Based 2D/2D Composite Heterojunction Photocatalyst. *Small Struct.* **2021**, *2*, 2100086. [CrossRef]

55. Fawy, K.F.; Ashiq, M.F.; Alharbi, F.F.; Manzoor, S.; Nisa, M.U.; Ibrahim, M.; Khan, M.T.N.; Messali, M.; Chughtai, A.H.; Ashiq, M.N. Facile synthesis of $NiMn_2O_4/ZnMn_2O_4$ heterostructure nanocomposite for visible-light-driven degradation of methylene blue dye. *J. Taibah Univ. Sci.* **2024**, *18*, 2302656. [CrossRef]

56. Azqandi, M.; Shahryari, T.; Fanaei, F.; Nasseh, N. Green construction of magnetic $MnFe_2O_4/ZIF$-8 nanocomposite utilizing extract of *Melissa officinalis* plant for the photo-degradation of tetracycline under UV illumination. *Catal. Commun.* **2023**, *185*, 106798. [CrossRef]

57. Xu, Q.L.; Wageh, S.; Al-Ghamdi, A.A.; Li, X. Design principle of S-scheme heterojunction photocatalyst. *J. Mater. Sci. Technol.* **2022**, *124*, 171–173. [CrossRef]

58. Fang, X.; Chen, J.; Zhan, J. Heterojunction photocatalyst for organic degradation: Superior photocatalytic activity through the phase and interface engineering. *Ceram. Int.* **2020**, *46*, 23245–23256. [CrossRef]

59. Luo, J.; Zhou, X.; Ma, L.; Xu, L.; Xu, X.; Du, Z.; Zhang, J. Enhancing visible light photocatalytic activity of direct Z-scheme SnS_2/Ag_3PO_4 heterojunction photocatalysts. *Mater. Res. Bull.* **2016**, *81*, 16–26. [CrossRef]

60. Zhang, B.; He, X.; Yu, C.Z.; Liu, G.C.; Ma, D.; Cui, C.Y.; Yan, Q.H.; Zhang, Y.J.; Zhang, G.S.; Ma, J.; et al. Degradation of tetracycline hydrochloride by ultrafine TiO_2 nanoparticles modified g-C_3N_4 heterojunction photocatalyst: Influencing factors, products and mechanism insight. *Chin. Chem. Lett.* **2022**, *33*, 1337–1342. [CrossRef]

61. Klongdee, J.; Petchkroh, W.; Phuempoonsathaporn, K.; Praserthdam, P.; Vangnai, A.; Pavarajarn, V. Activity of nanosized titania synthesized from thermal decomposition of titanium (IV) n-butoxide for the photocatalytic degradation of diuron. *Sci. Technol. Adv. Mater.* **2005**, *6*, 290–295. [CrossRef]

62. López-Ramón, M.V.; Rivera-Utrilla, J.; Sánchez-Polo, M.; Polo, A.M.S.; Mota, A.J.; Orellana-García, F.; Álvarez, M.A. Photocatalytic oxidation of diuron using nickel organic xerogel under simulated solar irradiation. *Sci. Total Environ.* **2019**, *650*, 1207–1215. [CrossRef] [PubMed]

63. Luan, J.F.; Hao, L.; Yao, Y.; Wang, Y.C.; Yang, G.M.; Li, J. Preparation and Property Characterization of $Sm_2EuSbO_7/ZnBiSbO_5$ Heterojunction Photocatalyst for Photodegradation of Parathion Methyl under Visible Light Irradiation. *Molecules* **2023**, *28*, 7722. [CrossRef] [PubMed]

64. Li, H.; Liu, C.; Li, K.; Wang, H. Preparation, characterization and photocatalytic properties of nanoplate Bi_2MoO_6 catalysts. *J. Mater. Sci.* **2008**, *43*, 7026–7034. [CrossRef]

65. Voronkova, V.I.; Kharitonova, E.P.; Rudnitskaya, O.G. Refinement of Bi_2WO_6 and Bi_2MoO_6 polymorphism. *J. Alloys Compd.* **2009**, *487*, 274–279. [CrossRef]

66. Li, H.; Liu, J.; Hou, W.; Du, N.; Zhang, R.; Tao, X. Synthesis and characterization of g-C_3N_4/Bi_2MoO_6 heterojunctions with enhanced visible light photocatalytic activity. *Appl. Catal. B* **2014**, *160–161*, 89–97. [CrossRef]

67. Zeng, X.; Shu, S.; Meng, Y.; Wang, H.; Wang, Y. Enhanced photocatalytic degradation of sulfamethazine by g-C_3N_4/Cu, N-TiO_2 composites under simulated sunlight irradiation. *Chem. Eng. J.* **2023**, *456*, 141105. [CrossRef]

68. Ariza-Tarazona, M.C.; Villarreal-Chiu, J.F.; Barbieri, V.; Siligardi, C.; Cedillo-González, E.I. New strategy for microplastic degradation: Green photocatalysis using a protein-based porous N-TiO_2 semiconductor. *Ceram. Int.* **2019**, *45*, 9618–9624. [CrossRef]

69. Keramati, N.; Nasernejad, B.; Fallah, N. Synthesis of N-TiO_2: Stability and Visible Light Activity for Aqueous Styrene Degradation. *J. Dispers. Sci. Technol.* **2014**, *35*, 1476–1482. [CrossRef]

70. Luan, J.F.; Li, M.; Ma, K.; Li, Y.M.; Zou, Z.G. Photocatalytic activity of novel Y_2InSbO_7 and Y_2GdSbO_7 nanocatalysts for degradation of environmental pollutant rhodamine B under visible light irradiation. *Chem. Eng. J.* **2011**, *167*, 162–171. [CrossRef]

71. Ait Ahsaine, H.; BaQais, A.; Arab, M.; Bakiz, B.; Benlhachemi, A. Synthesis and Electrocatalytic Activity of Bismuth Tungstate Bi_2WO_6 for Rhodamine B Electro-Oxidation. *Catalysts* **2022**, *12*, 1335. [CrossRef]

72. Mortazavi-Derazkola, S.; Salavati-Niasari, M.; Amiri, O.; Abbasi, A. Fabrication and characterization of $Fe_3O_4@SiO_2@TiO_2@Ho$ nanostructures as a novel and highly efficient photocatalyst for degradation of organic pollution. *J. Energy Chem.* **2017**, *26*, 17–23. [CrossRef]

73. Mortazavi-Derazkola, S.; Zinatloo-Ajabshir, S.; Salavati-Niasari, M. New facile preparation of Ho_2O_3 nanostructured material with improved photocatalytic performance. *J. Mater. Sci.-Mater. Electron.* **2016**, *28*, 1914–1924. [CrossRef]

74. Rada, S.; Rus, L.; Rada, M.; Zagrai, M.; Culea, E.; Rusu, T. Compositional dependence of structure, optical and electrochemical properties of antimony(III) oxide doped lead glasses and vitroceramics. *Ceram. Int.* **2014**, *40*, 15711–15716. [CrossRef]

75. Kaviyarasu, K.; Sajan, D.; Devarajan, P.A. A rapid and versatile method for solvothermal synthesis of Sb_2O_3 nanocrystals under mild conditions. *Appl. Nanosci.* **2012**, *3*, 529–533. [CrossRef]

76. Satheesh Kumar, R.; Ponnusamy, V.; Jose, M.T. Synthesis and photoluminescence properties of Sm^{3+}-doped $YAl_3(BO_3)_4$ phosphor. *Luminescence* **2013**, *29*, 649–656. [CrossRef] [PubMed]

77. Phuruangrat, A.; Jitrou, P.; Dumrongrojthanath, P.; Ekthammathat, N.; Kuntalue, B.; Thongtem, S.; Thongtem, T. Hydrothermal Synthesis and Characterization of Bi_2MoO_6 Nanoplates and Their Photocatalytic Activities. *J. Nanomater.* **2013**, *2013*, 789705. [CrossRef]

78. Bahareh, K.; Habibi, M.H. High photocatalytic activity of light-driven Fe_2TiO_5 nanoheterostructure toward degradation of antibiotic metronidazole. *J. Ind. Eng. Chem.* **2019**, *80*, 292–300. [CrossRef]

79. Naidu, B.S.; Pandey, M.; Sudarsan, V.; Vatsa, R.K.; Tewari, R. Photoluminescence and Raman spectroscopic investigations of morphology assisted effects in Sb_2O_3. *Chem. Phys. Lett.* **2009**, *474*, 180–184. [CrossRef]

80. Lonappan, D.; Shekar, N.V.C.; Ravindran, T.R.; Sahu, P.C. High-pressure phase transition in Ho_2O_3. *Mater. Chem. Phys.* **2010**, *120*, 65–67. [CrossRef]

81. Zhu, W.; Wu, Y.; Leto, A.; Du, J.; Pezzotti, G. Cathodoluminescence and Raman Spectroscopic Analyses of Nd- or Yb-Doped Y_2O_3 Transparent Ceramics. *J. Phys. Chem. A* **2013**, *117*, 3599–3607. [CrossRef]

82. Li, H.H.; Li, K.W.; Wang, H. Hydrothermal synthesis and photocatalytic properties of bismuth molybdate materials. *Mater. Chem. Phys.* **2009**, *116*, 134–142. [CrossRef]

83. Zhang, L.W.; Xu, T.G.; Zhao, X.; Zhu, Y.F. Controllable synthesis of Bi_2MoO_6 and effect of morphology and variation in local structure on photocatalytic activities. *Appl. Catal. B-Environ.* **2010**, *98*, 138–146. [CrossRef]

84. Nowak, M.; Kauch, B.; Szperlich, P. Determination of energy band gap of nanocrystalline SbSI using diffuse reflectance spectroscopy. *Rev. Sci. Instrum.* **2009**, *80*, 046107. [CrossRef] [PubMed]

85. Zhou, F.; Kang, K.; Maxisch, T.; Ceder, G.; Morgan, D. The electronic structure and band gap of $LiFePO_4$ and $LiMnPO_4$. *Solid State Commun.* **2004**, *132*, 181–186. [CrossRef]

86. Tauc, J.; Grigorovici, R.; Vancu, A. Optical properties and electronic structure of amorphous germanium. *Phys. Status Solidi.* **1966**, *15*, 627–637. [CrossRef]

87. Butler, M.A.; Ginley, D.S.; Eibschutz, M. Photoelectrolysis with $YFeO_3$ electrodes. *J. Appl. Phys.* **1977**, *48*, 3070–3072. [CrossRef]

88. Makula, P.; Pacia, M.; Macyk, W. How To Correctly Determine the Band Gap Energy of Modified Semiconductor Photocatalysts Based on UV-Vis Spectra. *J. Phys. Chem. Lett.* **2018**, *9*, 6814–6817. [CrossRef] [PubMed]

89. Yao, Y.; Luan, J. Preparation, Property Characterization of $Gd_2YSbO_7/ZnBiNbO_5$ Heterojunction Photocatalyst for Photocatalytic Degradation of Benzotriazole under Visible Light Irradiation. *Catalysts* **2022**, *12*, 159. [CrossRef]

90. Liu, B.Y.; Du, J.Y.; Ke, G.L.; Jia, B.; Huang, Y.J.; He, H.C.; Zhou, Y.; Zou, Z.G. Boosting O_2 Reduction and H_2O Dehydrogenation Kinetics: Surface N-Hydroxymethylation of g-C_3N_4 Photocatalysts for the Efficient Production of H_2O_2. *Adv. Funct. Mater.* **2022**, *32*, 2111125. [CrossRef]

91. Liu, C.; Feng, Y.; Han, Z.T.; Sun, Y.; Wang, X.Q.; Zhang, Q.F.; Zou, Z.G. Z-scheme N-doped $K_4Nb_6O_{17}$/g-C_3N_4 heterojunction with superior visible-light-driven photocatalytic activity for organic pollutant removal and hydrogen production. *Chin. J. Catal.* **2021**, *42*, 164–174. [CrossRef]

92. Wang, L.; Wang, J.; Fei, Y.; Cheng, H.; Pan, H.; Wu, C. Ag_3PO_4/Bi_2WO_6 Heterojunction Photocatalyst with Remarkable Visible-Light-Driven Catalytic Activity. *Crystals* **2023**, *13*, 1531. [CrossRef]

93. Zhang, H.; Fan, Z.; Chai, Q.; Li, J. Facile Synthesis of a Bi_2WO_6/BiO_{2-x} Heterojunction for Efficient Photocatalytic Degradation of Ciprofloxacin under Visible Light Irradiation. *Catalysts* **2023**, *13*, 469. [CrossRef]

94. Liu, A.Y.; Hu, J.Q.; He, J.L.; Huang, X.Y.; Hu, N.; Li, Y.Q.; Huang, Q.L.; Guo, S.; Liu, X.; Yang, Z.; et al. Direct Z-scheme hierarchical heterostructures of oxygen-doped g-C_3N_4/In_2S_3 with efficient photocatalytic Cr(vi) reduction activity. *Catal. Sci. Technol.* **2021**, *11*, 7963–7972. [CrossRef]

95. Bano, N.; Manzoor, S.; Sami, A.; Shah, S.I.A.; Junaid, A.; Rehman, M.Y.U.; Alshgari, R.A.; Ehsan, M.F.; Ashiq, M.N. Fabrication of vanadium telluride anchored on carbon nanotubes nanocomposite for overall water splitting. *J. Am. Ceram. Soc.* **2024**, *107*, 4027–4041. [CrossRef]

96. Ahmad, W.; Shahzadi, I.; Haider, A.; Ul-Hamid, A.; Ullah, H.; Khan, S.; Somaily, H.H.; Ikram, M. Efficient Dye Degradation and Antimicrobial Behavior with Molecular Docking Performance of Silver and Polyvinylpyrrolidone-Doped Zn-Fe Layered Double Hydroxide. *ACS Omega* **2024**, *9*, 5068–5079. [CrossRef]

97. Ikram, M.; Naz, M.; Haider, A.; Shahzadi, I.; Mehboob, H.U.; Bari, M.A.; Ul-Hamid, A.; Algaradah, M.M.; Al-Anazy, M.M. Carbon sphere doped CdS quantum dots served as a dye degrader and their bactericidal behavior analysed with in silico molecular docking analysis. *Nanoscale Adv.* **2023**, *6*, 233–246. [CrossRef] [PubMed]

98. Panahi, A.H.; Al-Musawi, T.J.; Masihpour, M.; Fard, S.F.T.; Nasseh, N. Photocatalytic Degradation of Humic Acid Using Bentonite@Fe_3O_4@ZnO Magnetic Nanocomposite: An Investigation of the Characterization of the Photocatalyst, Degradation Pathway, and Modeling by Solver Plugin. *Water* **2023**, *15*, 2931. [CrossRef]

99. Zhuang, Y.; Luan, J.F. Improved photocatalytic property of peony-like InOOH for degrading norfloxacin. *Chem. Eng. J.* **2020**, *382*, 122770. [CrossRef]

100. Dvoranová, D.; Brezová, V.; Mazúr, M.; Malati, M.A. Investigations of metal-doped titanium dioxide photocatalysts. *Appl. Catal. B-Environ.* **2002**, *37*, 91–105. [CrossRef]

101. Balakrishnan, G.; Velavan, R.; Mujasam Batoo, K.; Raslan, E.H. Microstructure, optical and photocatalytic properties of MgO nanoparticles. *Results Phys.* **2020**, *16*, 103013. [CrossRef]

102. Ali, T.; Tripathi, P.; Azam, A.; Raza, W.; Ahmed, A.S.; Ahmed, A.; Muneer, M. Photocatalytic performance of Fe-doped TiO_2 nanoparticles under visible-light irradiation. *Mater. Res. Express* **2017**, *4*, 015022. [CrossRef]

103. Chen, J.; Zhao, X.; Kim, S.G.; Park, N.G. Multifunctional Chemical Linker Imidazoleacetic Acid Hydrochloride for 21% Efficient and Stable Planar Perovskite Solar Cells. *Adv. Mater.* **2019**, *31*, 1902902. [CrossRef] [PubMed]

104. Gao, Z.W.; Wang, Y.; Ouyang, D.; Liu, H.; Huang, Z.F.; Kim, J.; Choy, W.C.H. Triple Interface Passivation Strategy-Enabled Efficient and Stable Inverted Perovskite Solar Cells. *Small Methods* **2020**, *4*, 2000478. [CrossRef]

105. Chen, J.; Kim, S.-G.; Ren, X.; Jung, H.S.; Park, N.-G. Effect of bidentate and tridentate additives on the photovoltaic performance and stability of perovskite solar cells. *J. Mater. Chem. A* **2019**, *7*, 4977–4987. [CrossRef]

106. Cheng, Y.X.; Ye, J.H.; Lai, L.; Fang, S.; Guo, D.Y. Ambipolarity Regulation of Deep-UV Photocurrent by Controlling Crystalline Phases in Ga_2O_3 Nanostructure for Switchable Logic Applications. *Adv. Electron. Mater.* **2023**, *9*, 2201216. [CrossRef]

107. Ma, Q.; Kumar, R.K.; Xu, S.Y.; Koppens, F.H.L.; Song, J.C.W. Photocurrent as a multiphysics diagnostic of quantum materials. *Nat. Rev. Phys.* **2023**, *5*, 170–184. [CrossRef]

108. Behera, A.; Mansingh, S.; Das, K.K.; Parida, K. Synergistic $ZnFe_2O_4$-carbon allotropes nanocomposite photocatalyst for norfloxacin degradation and Cr (VI) reduction. *J. Colloid Interface Sci.* **2019**, *544*, 96–111. [CrossRef]

109. Bredar, A.R.C.; Chown, A.L.; Burton, A.R.; Farnum, B.H. Electrochemical Impedance Spectroscopy of Metal Oxide Electrodes for Energy Applications. *ACS Appl. Energy Mater.* **2020**, *3*, 66–98. [CrossRef]

110. Annadi, A.; Gong, H. Success in both p-type and n-type of a novel transparent AgCuI alloy semiconductor system for homojunction devices. *Appl. Mater. Today* **2020**, *20*, 100703. [CrossRef]

111. Xu, S.; Gong, S.; Jiang, H.; Shi, P.; Fan, J.; Xu, Q.; Min, Y. Z-scheme heterojunction through interface engineering for broad spectrum photocatalytic water splitting. *Appl. Catal. B* **2020**, *267*, 118661. [CrossRef]

112. Cheng, T.; Gao, H.; Sun, X.; Xian, T.; Wang, S.; Yi, Z.; Liu, G.; Wang, X.; Yang, H. An excellent Z-scheme $Ag_2MoO_4/Bi_4Ti_3O_{12}$ heterojunction photocatalyst: Construction strategy and application in environmental purification. *Adv. Powder Technol.* **2021**, *32*, 951–962. [CrossRef]

113. Barrocas, B.T.; Ambrozova, N.; Koci, K. Photocatalytic Reduction of Carbon Dioxide on TiO_2 Heterojunction Photocatalysts—A Review. *Materials* **2022**, *15*, 967. [CrossRef]

114. Huang, W.; Li, Y.F.; Fu, Q.M.; Chen, M. Fabrication of a novel biochar decorated nano-flower-like MoS_2 nanomaterial for the enhanced photodegradation activity of ciprofloxacin: Performance and mechanism. *Mater. Res. Bull.* **2022**, *147*, 111650. [CrossRef]

115. Yan, S.W.; Yang, J.; Li, Y.; Jia, X.H.; Song, H.J. One-step synthesis of ZnS/BiOBr photocatalyst to enhance photodegradation of tetracycline under full spectral irradiation. *Mater. Lett.* **2020**, *276*, 128232. [CrossRef]

116. Zhang, J.F.; Hu, Y.F.; Jiang, X.L.; Chen, S.F.; Meng, S.G.; Fu, X.L. Design of a direct Z-scheme photocatalyst: Preparation and characterization of $Bi_2O_3/g\text{-}C_3N_4$ with high visible light activity. *J. Hazard. Mater.* **2014**, *280*, 713–722. [CrossRef] [PubMed]

117. Katsumata, H.; Sada, M.; Nakaoka, Y.; Kaneco, S.; Suzuki, T.; Ohta, K. Photocatalytic degradation of diuron in aqueous solution by platinized TiO_2. *J. Hazard. Mater.* **2009**, *171*, 1081–1087. [CrossRef] [PubMed]

118. Mestankova, H.; Escher, B.; Schirmer, K.; von Gunten, U.; Canonica, S. Evolution of algal toxicity during (photo)oxidative degradation of diuron. *Aquat. Toxicol.* **2011**, *101*, 466–473. [CrossRef]

119. Mazellier, P.; Jirkovsky, J.; Bolte, M. Degradation of diuron photoinduced by iron(III) in aqueous solution. *Pestic. Sci.* **1997**, *49*, 259–267. [CrossRef]

120. Macounová, K.; Krysová, H.; Ludvík, J.; Jirkovsky, J. Kinetics of photocatalytic degradation of diuron in aqueous colloidal solutions of Q-TiO_2 particles. *J. Photochem. Photobiol. A* **2003**, *156*, 273–282. [CrossRef]

121. Malato, S.; Cáceres, J.; Fernández-Alba, A.R.; Piedra, L.; Hernando, M.D.; Agüera, A.; Vial, J. Photocatalytic treatment of diuron by solar photocatalysis: Evaluation of main intermediates and toxicity. *Environ. Sci. Technol.* **2003**, *37*, 2516–2524. [CrossRef]